

CHAPTER 4

Bainite Transformation Kinetics & the Non-Uniform Distribution of Carbon

4.1 Introduction

Bainite in steels tends to grow in the form of clusters of small, parallel plates known as 'sub-units', each of a limited size and with all sub-units within a particular sheaf having the same crystallographic orientation (Bhadeshia & Christian, 1990; Christian & Edmonds, 1984). The individual plates within a sheaf, although interconnected in three dimensions, can be separated along most of their surfaces by thin films of untransformed austenite especially in steels where carbide precipitation reactions are suppressed (it is these steels that are considered here) (Bhadeshia & Christian, 1990; Christian & Edmonds, 1984). This is in contrast to the large blocks of austenite which may remain untransformed as bainite sheaves growing in different directions impinge on one another. Figure 4.1 shows untransformed austenite regions of both types.

The maximum extent of the bainite reaction in steels is limited by the carbon which diffuses from the supersaturated bainitic ferrite plates into the untransformed austenite immediately after transformation. Such steels are of considerable technological importance, both from the point of view of ultra high strength alloys and welding alloys. The partitioned carbon enriches the austenite to such a degree as reaction proceeds, that the driving force for transformation eventually reaches zero. The reaction then stops, even though substantial amounts of untransformed austenite remain in the microstructure.

Bainite transformation kinetics have in the past been calculated assuming that the carbon is homogeneously distributed in the residual austenite, but there is now considerable evidence to suggest that this is not the case. The films of austenite between the ferrite plates are to a large extent, isolated by the surrounding ferrite. They can achieve carbon concentration levels which are far in excess of the levels expected assuming a homogeneous distribution. Such 'trapping' of excess carbon in the isolated films would intuitively be expected to lead to a larger maximum volume fraction of ferrite, since the carbon concentration in the larger blocks of untransformed austenite will be correspondingly smaller at any stage of reaction. There is some experimental evidence for this. Continuous cooling experiments in which the cooling rate is so slow that there is a greater opportunity for partitioned carbon to homogenise, show that a larger degree of transformation is obtained when the carbon is inhomogeneously distributed (Khan & Bhadeshia, 1990).

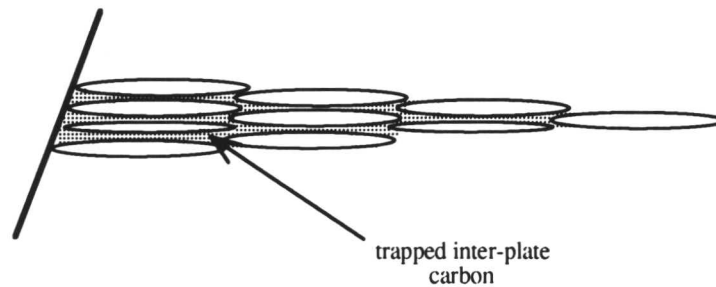
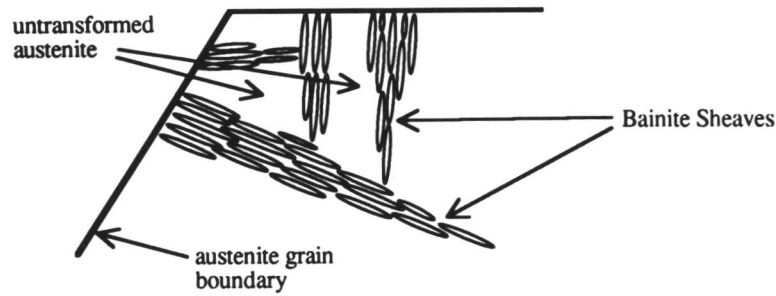


Figure 4.1 Schematic diagrams indicating the location of untransformed austenite in bainitic microstructure. a) Blocky regions of austenite between sheaves. b) Thin films of carbon enriched austenite between bainitic sub-units.

The purpose of this work is to examine theoretically, the extent to which the trapping phenomenon influences both the kinetics and the maximum extent of transformation that can be achieved at any temperature, using the theory developed in Chapter 3. The modifications and improvements made to the original kinetic theory are incorporated and extended in this chapter.

4.2 Accounting for the Trapping of Carbon

The treatment of bainite kinetics as presented in Chapter 3 supposes that the carbon that is rejected from the transformed bainitic ferrite is homogeneously distributed in the untransformed austenite. In reality, some of the austenite is in the form of isolated films between the plates of ferrite. The carbon that diffuses into these films becomes trapped there and should therefore change the way in which the reaction proceeds. A modification is presented below which takes

account of the expected inhomogeneous distribution of carbon.

Some simplifying assumptions are necessary. It is assumed that one film of austenite is trapped for each sub-unit of bainite that grows. It is well established that the films trapped within sheaves are carbon-enriched to concentrations which are in general much larger than that expected from the T'_0 curve (explained in Chapter 3). Therefore, it is assumed that the films are saturated with carbon. The composition of the austenite films is then given by the value of the Ae'_3 curve at the reaction temperature. (This is the composition of austenite at the paraequilibrium $\alpha + \gamma/\gamma$ phase boundary). The paraequilibrium phase boundary is chosen because no substitutional alloying element partitioning occurs during bainite formation. Considering a unit volume of austenite, a volume u is assigned to each bainitic sub-unit, and a volume v_t to each film of trapped austenite.

By a mass balance argument the carbon content x_B of the untransformed blocky austenite after n plates of ferrite have formed in a unit volume of sample, (*i.e.* when the volume fraction of ferrite is nu) is:

$$x_B = \frac{\bar{x} - nu[x_\alpha + (v_t/u)x_{Ae'_3}]}{1 - nu[1 + (v_t/u)]} \quad (4.1)$$

where \bar{x} is the mean carbon content of the the alloy; x_α is the carbon concentration of the ferrite; $x_{Ae'_3}$ is the carbon content of the austenite saturated with carbon.

The reaction of austenite to ferrite will cease when the composition of the austenite has reached the T'_0 value (Christian & Edmonds, 1984; Khan & Bhadeshia, 1990). This is the carbon concentration at which ferrite with a strain energy of 400 J mol^{-1} has the same free energy of as austenite of the same composition, which therefore makes it the limiting austenite composition that can support transformation to bainite.

By rearrangement of the above expression a maximum allowable volume θ' can be calculated. This corresponds to the condition where the carbon concentration of the blocky austenite has reached the T'_0 value.

$$\theta' = \frac{\bar{x} - x_{T'_0}}{[x_\alpha + (v_t/u)x_{Ae'_3}] - [1 - (v_t/u)x_{T'_0}]} \quad (4.2)$$

It is possible however, for the austenite to become enriched in carbon to such an extent that the *nucleation* of ferrite by a displacive mechanism is impossible, before the carbon content of the austenite reaches $x_{T'_0}$ (which is the determined by driving force for bainite growth). Under these conditions, if x_{N_0} represents the carbon content at which nucleation ceases then the maximum allowable extent of transformation is

$$\theta' = \frac{\bar{x} - x_{N_0}}{[x_\alpha + (v_t/u)x_{Ae'_3}] - [1 - (v_t/u)x_{N_0}]} \quad (4.3)$$

Regardless of whether the termination of reaction occurs because the available driving force is insufficient for nucleation or for growth it is convenient to express the mole fraction of ferrite in terms of a normalised volume fraction:

$$\xi' = v/\theta' \quad (4.4)$$

where, as demonstrated above, the actual volume fraction of ferrite $v = nu$.

4.3 Computational Details

The assumption that all films are of identical volume is of course an approximation. It is difficult to estimate the relative thicknesses of the plates and films in a meaningful way, since bainitic plates often touch along some of their surfaces. A series of hypothetical values are therefore used to represent the film thickness so that the sensitivity of the predicted transformation rate to the trapping effect can be investigated.

Calculations were performed for three hypothetical steels of different carbon and substitutional solute content (Table 4.1). Since it is anticipated that carbon trapping will affect both the driving force and the allowable extent of reaction it is of interest to perform calculations comparing reactions for two cases:

- (a) alloys with different carbon levels but with the same driving force;
- (b) two alloys with the same carbon content, but different driving force.

Alloy No.	C	Si	Mn
A1	0.1	2.0	2.0
A2	0.2	2.0	1.87
A3	0.1	2.0	1.5

Table 4.1 Compositions (wt.%) of the steels chosen for investigating the predicted effect of trapping of carbon in retained austenite films.

Alloy A2 was chosen to have the same driving force as alloy A1 at 500°C so that special consideration could be given to the relative reaction rates at this temperature. Alloy A3 has the same carbon content in weight percent as alloy A1, though the mole fraction of carbon will be slightly different for the two alloys. The important thermodynamic quantities for the three alloys at 500°C are shown in Table 4.2. For all three alloys at this temperature it was found that $x_{T'_0}$ was less than x_{N_0} . Termination of reaction will therefore be due to a failure of the thermodynamic criterion for growth in all three cases. The maximum extent of transformation is therefore calculated using $x_{T'_0}$.

It is also noteworthy that the maximum allowable fraction of ferrite for alloys A1 and A2 will be different at 500°C since the carbon content is different. Carbon can also affect the reaction kinetics by altering the auto-catalysis factor. It is therefore anticipated that the trapping phenomenon will affect the lower carbon alloy to a greater extent than for the higher carbon alloys, since a greater fraction of the total carbon will be trapped in the thin film austenite.

Alloy No.	$\Delta G_m^0/\text{J mol}^{-1}$	β	\bar{x} (at. frac.)	$x_{T_0'}$ (at. frac.)	$x_{Ae_3'}$ (at. frac.)
A1	-880	148.79	4.541×10^{-3}	1.396×10^{-3}	5.678×10^{-3}
A2	-880	125.12	9.050×10^{-3}	1.447×10^{-3}	5.194×10^{-3}
A3	-996	148.78	4.542×10^{-3}	1.673×10^{-3}	6.582×10^{-3}

Table 4.2 Comparison of parameters affecting the predicted kinetics of the bainite transformation at 500°C. The values are independent of the effect of trapping of carbon, and account for some of the differences in transformation rate shown in Figure 4.2

4.4 Results

Figure 4.2 shows the calculated effect of the presence of trapped high-carbon austenite films on the predicted reaction profiles of alloys A1, A2 and A3 at 500°C. Table 4.2 gives the values of the important parameters from the bainite reaction kinetics theory for these three steels at the reaction temperature, so that a comparison can be made. Four different film thicknesses are considered, with values such that

$$v_i/u = 0.005, 0.01, 0.015, 0.02$$

The reason for choosing these particular values is that it was hoped to investigate the effect of trapping of carbon while avoiding the condition in which *all* the carbon partitioned from the bainitic ferrite was trapped in the austenite films.

4.5 Discussion

Examination of the results in Figure 4.2 shows that for steels with equal driving forces at the same transformation temperature the carbon content of the alloy determines the magnitude of the effect of trapping. The extent of reaction and the transformation kinetics are affected to a greater degree in the lowest carbon alloy, with the effect of carbon on the auto-catalysis factor greatly affecting the overall transformation rate. For steels with similar carbon content but

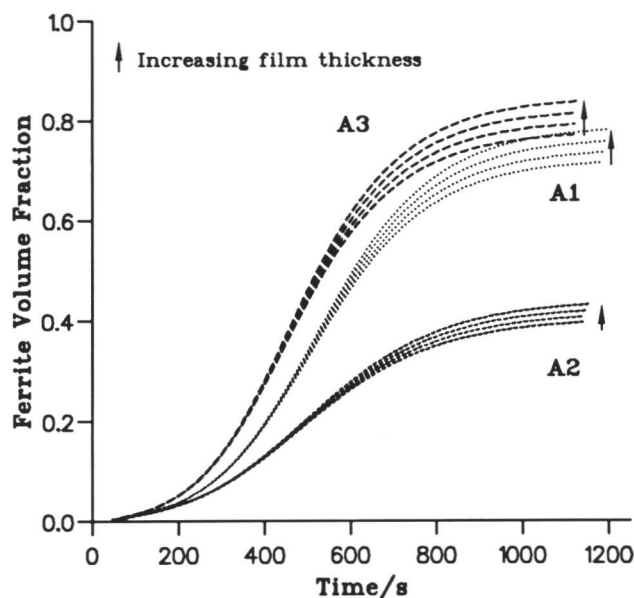


Figure 4.2 The calculated effect of the presence of trapped austenite films on the bainite kinetics of the three hypothetical steels whose compositions are listed in Table 4.1

different driving force the effect of trapping on the extent of transformation is very similar. In these cases the different reaction kinetics are mainly a result of the difference in driving force, since the effect of auto-catalysis is the same in both alloys. Though the fraction of carbon trapped in the two steels is dependent on the respective Ae'_3 compositions, it appears that the magnitude of the effect is similar in both cases.

Intuition suggests that the presence of trapped films will have the largest effect on the extent of transformation and the kinetics of transformation for the low carbon alloy in the series being investigated. This is because, with the film composition set equal to the Ae'_3 composition a larger fraction of the total carbon content of the alloy will be trapped.

The trend in the calculations that the reaction is faster for the case of the larger film thickness *i.e.* the larger the amount of carbon that is trapped, the faster the reaction proceeds. The limiting case is when the film thickness is related to the phase compositions by the expression

$$\frac{v_t}{u} = \frac{\bar{x} - x_\alpha}{x_{Ae'_3}}$$

since this represents the condition when all carbon partitioned by the ferrite ends up in the thin-film austenite. Since, under this condition there will be no enrichment of bulk untrans-

formed austenite, reaction can proceed until all the bulk austenite is consumed. The resulting microstructure would then consist solely of bainitic ferrite and thin film carbon-enriched austenite.

Considering the effect of trapping on the maximum extent of the bainite reaction for the series of alloys shows that the magnitude of the increase in maximum volume fraction produced by the inhomogeneous distribution of carbon does not vary significantly with substitutional alloying element concentration. This is to be expected, because the effect of trapping is mainly dependent on the proportion of the total carbon that is trapped. The substitutional alloying element concentration can affect the T'_0 and N_0 compositions, but terms such as these are mainly dependent on driving force, so that their effect should be hidden when a comparison is made at constant driving force.

The higher carbon steels show less sensitivity to the presence of trapped carbon. A smaller fraction of the total carbon is trapped between the sub-units in these cases. The maximum possible extent of transformation is also smaller. Consequently, the number of sheaves and the the corresponding number of austenite films available for trapping is reduced.

4.6 Conclusions

The non-uniform distribution of carbon due to the trapping of carbon in isolated austenite films leads to an acceleration of transformation. It further leads to an increase in the limiting fraction of bainitic ferrite that can be obtained at any temperature. Steels that have low carbon content are shown to be more sensitive to trapping effect because a greater fraction of the total carbon can then be accommodated in the films.

Carbide precipitation from austenite is most likely to occur from the film austenite which is richer in carbon. The present model could in fact be used to estimate the effect of such carbide precipitation of transformation kinetics. The carbides in effect remove carbon from the austenite, in a manner similar to the way in which the films of austenite isolate excess carbon from the reacting bulky regions of austenite.

CHAPTER 5

The Microstructure of High Strength Steel Welds

5.1 Background

A programme of research has been carried out (Svensson & Bhadeshia, 1988; Bhadeshia & Svensson, 1989) with the aim of producing a tough, high strength steel multi-pass weld, to be fabricated by the submerged arc, or the core continuous wire process. A novel approach to solving this problem was devised by the authors. In order to achieve good toughness it was desired to eliminate the detrimental phases, allotriomorphic ferrite and Widmanstätten ferrite from the microstructure, since these phases are relatively brittle. Other significant proposals for controlling the weld microstructure were also made, as discussed below.

It has been demonstrated the the toughness of the primary weld deposit shows greater scatter if the microstructure consists of more than one phase. The presence of Widmanstätten ferrite and allotriomorphic ferrite together with acicular ferrite therefore increases the scatter in toughness as well as decreasing the mean toughness. Tweed & Knott (1987) also suggest that toughness is improved by mechanical homogeneity in the weld, which implies that microstructural homogeneity is beneficial. Since many desired welds are multi-pass deposits it was necessary to ensure that the properties of the reheated regions of the weld are essentially similar to those of the primary weld metal.

In order to achieve this goal of uniform mechanical properties in multi pass welds it was proposed by Bhadeshia & Svensson that the composition of the weld deposit should be chosen so that the Ae'_3 temperature is reduced. This increases the tendency of the reheated regions to reaustenitise, and to transform to a microstructure similar to that of the primary regions on subsequent cooling. In order to ensure that regions of the weld that do not reaustenitise are not adversely affected by reheating, good temper resistance of the microstructure was considered essential.

In order to produce the high weld metal strength it was necessary to aim for a microstructure of acicular ferrite and martensite. A microstructure of acicular ferrite alone (*i.e.* with a very small fraction of martensitic microphases) cannot produce weld metal strength greater than ≈ 700 MPa. Since martensite can have a detrimental effect on the toughness of a weld deposit it was necessary to lower the carbon content of the alloys in order to avoid the formation of relatively brittle high-carbon twinned martensite. The partitioning of carbon in to the untransformed austenite as a result of the formation of ferrite at higher temperatures means that the martensite that forms will have a higher carbon content than the bulk alloy. Carbides forming within tempered martensite can help nucleate cleavage cracks and voids. Low carbon

martensite has the added advantage of a better temper resistance *i.e.* a reduced tendency to form carbides on tempering, since the martensitic ferrite then forms with a lower carbon supersaturation. The presence of silicon in the microstructure also helps inhibit cementite formation. Any loss of strength from the tempering process will be decreased if the temper resistance of the weld is increased, thereby improving the mechanical homogeneity of the weld.

The approach to the problem of developing a tough high-strength uniform weld was therefore to use intelligent additions of alloying elements to achieve the simultaneous goals of lowering the Ae'_3 temperature, producing a microstructure of acicular ferrite and martensite in the primary and re-austenitised regions, lowering the carbon content of martensite, and increasing the temper resistance of the microstructure as a whole.

Using the weld microstructure model a series of compositions were predicted as giving primary weld deposits with volume fractions of allotriomorphic ferrite and Widmanstätten ferrite of zero, or close to zero. The microstructure of this type of weld is therefore predicted as consisting of a mixture of acicular ferrite and 'microphases' only. The term 'microphases' is misleading in this context, since the fraction of acicular ferrite in the series is approximately 0.5. The relatively high hardenability of the steels selected suggests that any austenite remaining untransformed after the acicular ferrite reaction will decompose to martensite. This was confirmed by Bhadeshia & Svensson (1988) using transmission electron microscopy (TEM), in their preliminary examination of an experimental weld from this series. Hardness traverses across the fusion boundary in the experimental weld revealed that strength was maintained well as the microstructure changed from the as-deposited to the re-austenitised or tempered regions.

5.2 The Problem

The effect of increasing the substitutional alloy content on the microstructure of low alloy steel deposits is shown schematically in Figure 5.1. The weld microstructure model developed by Bhadeshia, Svensson and Grefott (1986-1991) determines the volume fraction of acicular ferrite by difference *i.e.* since, apart from a small amount of martensite, it is the last phase to form, its fraction can be determined by subtracting the fractions of the other phases from unity.

$$V_{\alpha_a} = 1 - V_{\alpha} - V_{\alpha_W} - V_m$$

where the subscripts α_a , α_W and m denote acicular ferrite, Widmanstätten ferrite and microphases including martensite. This method of determining the acicular ferrite content assumes that the fraction of martensite and other microphases can be estimated by thermodynamic approximations.

If the concentration of austenite stabilising elements is sufficiently large, transformation temperatures are depressed to such an extent that reconstructive transformations are too slug-

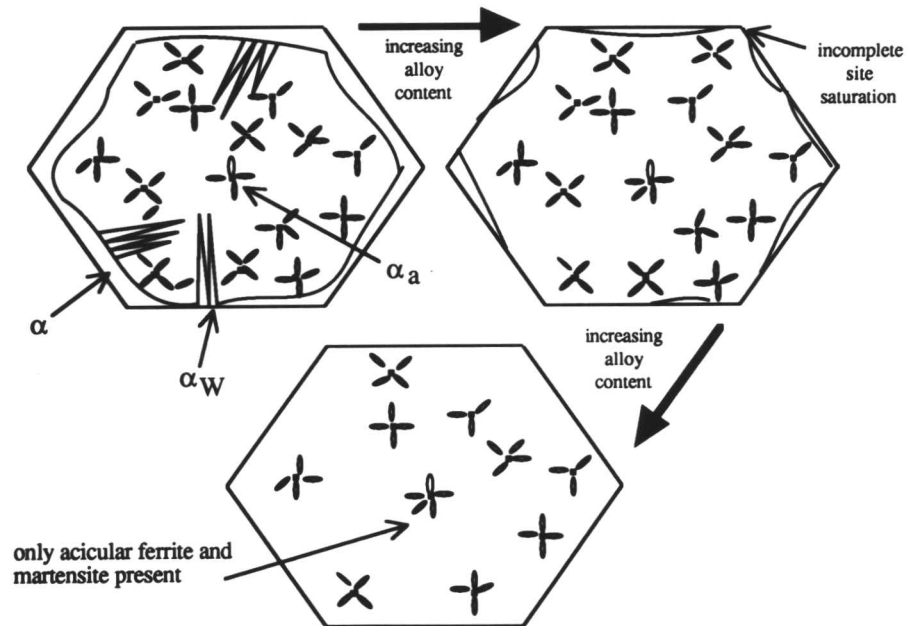


Figure 5.1 A schematic representation of the effect of increasing the austenite stabilising substitutional solute content on the the microstructure of low alloy steel welds.

gish to occur within the time scale of the cooling of the weld. Allotriomorphic ferrite will not then be present. By further alloying, the temperature at which displacive nucleation becomes possible is also lowered beneath that at which ferrite can grow by a displacive mechanism (Bhadeshia 1981a). This means that the formation of Widmanstätten ferrite does not occur, since by the time the nucleation of this phase becomes possible, it will possible to form bainite and acicular ferrite. It is expected, though, that further alloying will affect the relative volume fractions of acicular ferrite and martensite in the microstructure.

Since martensite and acicular ferrite have different properties, the strength and toughness of the weld is expected to be dependent on the relative volume fractions of these phases. Modelling of the microstructure is therefore of great potential importance in assessing and predicting the mechanical properties of the weld. An aim of the present work was to characterise the microstructure of welds of systematically varying chemistry in order to establish an experimental database of use in testing a microstructure prediction model.

5.3 Experimental Techniques

5.3.1 Materials

A series of ten experimental welds were provided by ESAB AB (Sweden), with a systematic

variation in the alloying element concentrations. The compositions of the welds are given in Table 5.1 with the dominant variation highlighted. Alloy 90 is the weld originally investigated by Bhadeshia & Svensson and its composition is included for comparison. Alloy 112 essentially reproduces that chemistry. Also of considerable interest is the trace element content of the welding alloys. The concentrations of oxygen, nitrogen, aluminium, titanium and sulphur are listed in Table 5.2. Trace element variations are expected to lead to differences in the inclusion chemistries of the welds, the chemistry being a possible source of microstructural variation via the nucleation of acicular ferrite. The welding parameters used in fabrication are listed in Table 5.3.

Alloy No.	C	Si	Mn	Ni	Mo	Cr	V
90	0.07	0.3	1.22	2.02	0.39	0.49	0.008
112	0.062	0.26	1.30	2.18	0.38	0.44	0.00
113	0.059	0.47	1.48	2.00	0.37	0.63	0.00
114	0.079	0.53	1.64	2.32	0.42	0.69	0.00
115	0.059	0.48	2.02	2.20	0.41	0.65	0.025
116	0.053	0.46	1.08	2.20	0.41	0.65	0.022
117	0.054	0.46	1.53	3.01	0.41	0.66	0.022
118	0.052	0.44	1.51	1.52	0.41	0.66	0.022
119	0.067	0.47	1.53	2.13	0.57	0.64	0.022
120	0.052	0.44	1.58	2.18	0.24	0.64	0.020
121	0.052	0.42	1.51	2.23	0.41	0.90	0.022
122	0.054	0.43	1.56	2.30	0.42	0.36	0.021

Table 5.1 Compositions of the alloys in the high strength weld series. All compositions are in wt%. Highlighted numbers indicate the major changes in chemistry relative to alloy 112.

5.4 Characterisation of the Weld Microstructure

5.4.1 Comparison of Microscopic Techniques

Optical Microscopy

Optical microscopy proved ineffective in characterising the microstructure of the welds in the experimental series. The scale of the microstructure is fine and the appearance of the two phases, acicular ferrite and martensite, both being plate-like, is too similar to be easily differentiated. Figure 5.2 shows an example of an optical micrograph of alloy 113 (centre bead,

Alloy No.	O	N	Al	Ti	S
90	322	76	200	40	70
112	363	81	220	40	60
113	304	55	220	60	50
114	267	47	220	70	60
115	358	56	150	20	50
116	356	45	150	20	50
117	398	52	150	20	50
118	411	49	140	20	50
119	415	52	180	20	50
120	481	50	150	20	50
121	468	52	150	20	50
122	397	46	150	20	50

Table 5.2 The trace element composition (ppm by weight) of the welding alloy series.

Alloy No.	Current/A	Voltage/V	Speed/m hour ⁻¹	Interpass Temperature/°C
90	580	29	33	200
112	580	29	33	200
113	500	29	30	200-250
114	500	29	30	200-250
115	500	29	30	200-250
116	500	29	30	200-250
117	500	29	30	200-250
118	500	29	30	200-250
119	500	29	30	200-250
120	500	29	30	200-250
121	500	29	30	200-250
122	500	29	30	200-250

Table 5.3 Welding variable values for the alloy series. All weld were made by the submerged arc process.

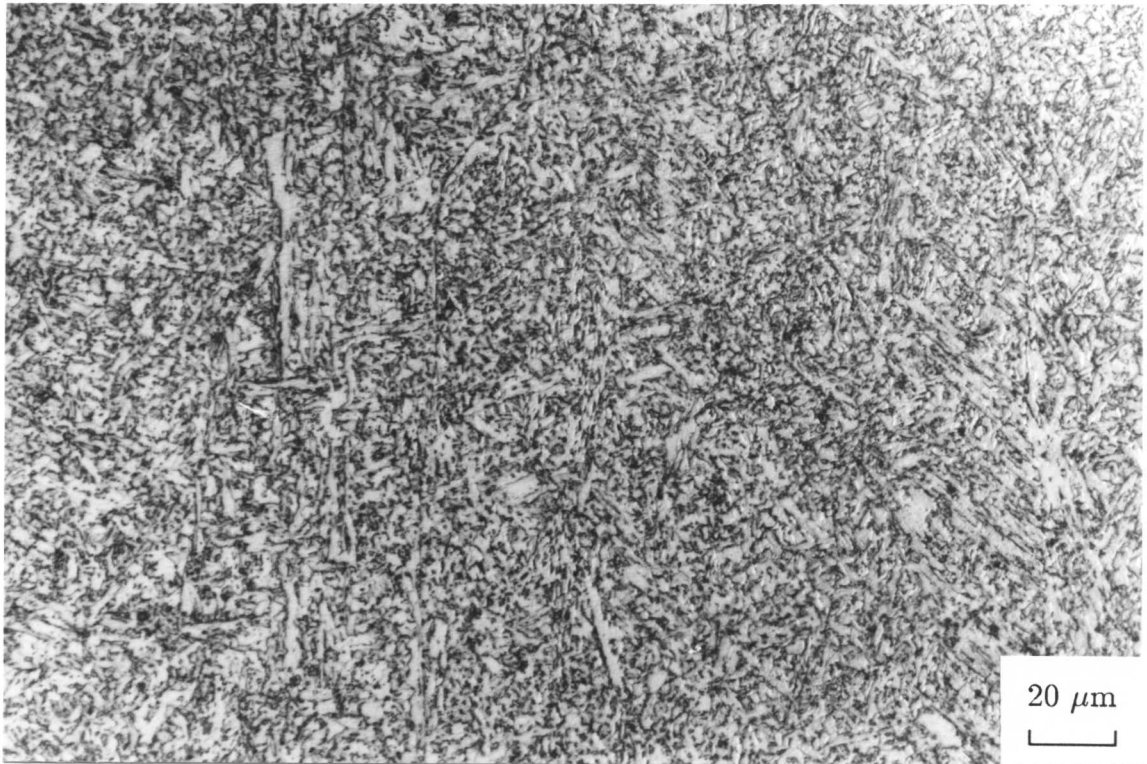


Figure 5.2 A typical optical micrograph of the structure of alloy 113, illustrating the difficulty in resolving the ultra-fine microstructure.

top layer). As can be seen, there is insufficient resolution to allow any quantitative estimation of the volume fractions of the phases present.

Scanning Electron Microscopy (SEM)

Conventional SEM images are difficult to interpret, but the use of the image inversion feature on the CAMSCAN S2 microscope enables a more easily recognisable microstructure to be seen. The reason for this is that by etching in nital, the acicular ferrite is attacked preferentially compared with the martensite, leaving the martensitic regions slightly elevated on the etched surface. Image inversion gives the appearance of raised acicular ferrite plates surrounded by martensite. SEM is the ideal instrument for recording microstructures at sufficiently high resolution for quantitative evaluation of the microstructural components while still enabling sufficiently large areas of the weld to be sampled so that local variations in the microstructure are taken into account. Great care was taken therefore to obtain the best possible SEM images of the welds.

Transmission Electron Microscopy (TEM)

The high magnification and resolution that TEM provides enables unambiguous identification of the microstructural components in the welds. A typical carbon replical TEM micrograph

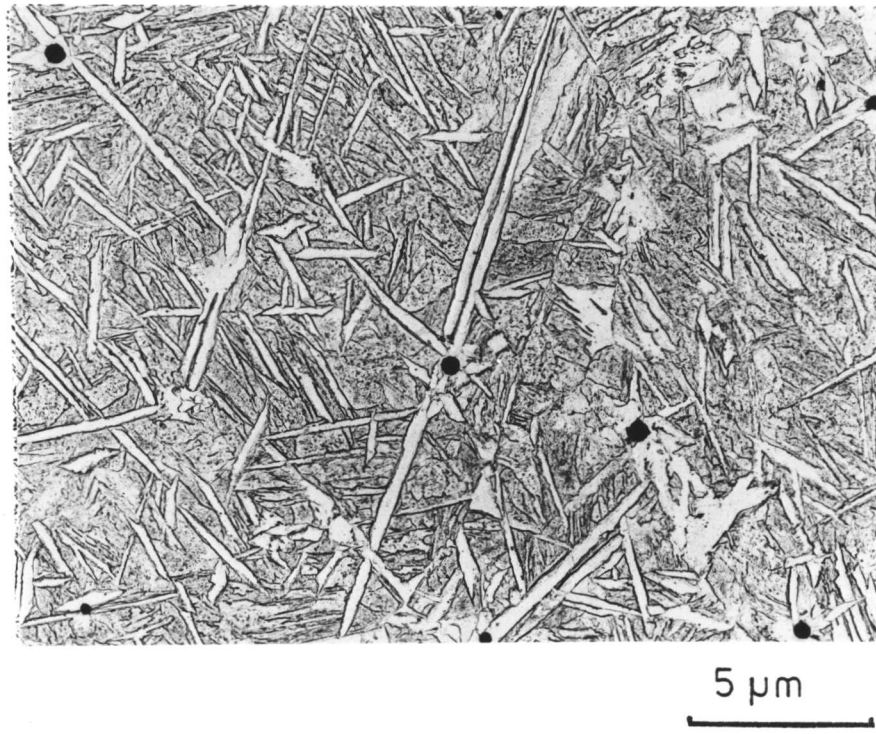


Figure 5.3 A typical carbon replica electron micrograph of the primary region of a steel weld deposit (after G.S. Barrite, 1982).

of an acicular ferrite and martensite structure is shown in Figure 5.3, where the different microstructural components are clearly distinguished. However, for the purpose of characterising and quantifying the microstructure of a weld, a large area needs to be sampled so that effects such as variations in acicular ferrite plate size, and the effect of chemical segregation can be examined. Investigation of weld microstructure on this scale makes TEM unsuitable. This can be illustrated by considering that Bhadeshia & Svensson approximated the volume fraction of acicular ferrite in alloy 90 to be around 0.4 using TEM, whereas SEM reveals a much higher fraction of this phase in the microstructure as a whole. Examination of SEM micrographs in this chapter demonstrates how, in many alloys, the occurrence of martensite islands is highly localised. Martensite islands of this kind occur in addition to the martensite which forms between acicular ferrite plates, and is probably a result of chemical segregation. The use of TEM could miss this important microstructural feature, simply by failing to sample a large enough area, even if many specimens were examined. Carbon replica work on TEM provides essentially similar results to SEM since it is the surface topography of etched specimens that is examined.

5.4.2 Microhardness Testing and Hardness Traverses

The microstructure of the high strength weld can also be characterised by the microhard-

ness of the primary weld deposit. Steels with a larger volume fraction of martensite are expected to have higher hardness values, though alloying element content and other factors can also affect hardness. A model which attempts to account for all the factors affecting the hardness of the primary weld deposit is presented in the following chapter. Trends in hardness can therefore be linked to trends in the volume fraction of the phases in the welds. Of great importance is the need for mechanically homogeneous welds, in which the absence of microstructural inhomogeneity imparts reproducibly good toughness which can be exploited successfully by reducing scatter. Microhardness traverses were performed across the fusion line of the primary weld bead into the reaustenitised and reheated regions of selected alloys in order to investigate any trends in properties that could result from refinement of austenite grain size, differences in cooling behaviour after reaustenitisation, and possible tempering effects. The alloys chosen for this investigation were alloys 119, 120, 121, 122 *i.e.* those with systematic variations in the concentration of molybdenum and chromium, elements which can cause secondary hardening.

5.4.3 *Microstructural Homogeneity*

A series of SEM micrographs was taken for two particular welds from the series, alloy 113 and alloy 114. The micrographs covered an area which included the columnar grained austenite region of the primary weld metal, into the equiaxed austenite grains of the reaustenitised region of the neighbouring bead. The reaustenitised regions of the weld were distinguished by the isotropic, equiaxed appearance of the austenite grains, with regions of columnar grains close to the reaustenitised material being interpreted as tempered.

The object of this exercise was to investigate any change in microstructure arising from the different austenite grain morphology; the reaustenitised weld metal can transform to bainite if the austenite grain size is sufficiently small *i.e.* the number density of grain boundary nucleation sites increases relative to the inclusion site density to cause grain boundary nucleation of bainite to dominate over the intragranular nucleation of acicular ferrite (Yang & Bhadeshia, 1987). The size to which an austenite grain will grow depends on the maximum temperature experienced, as well as on the kinetics of reaustenitisation. Other factors such as the pinning of the austenite grains by particles in the weld metal may also be important. The effect of the heat input on previously deposited metal decreases with distance from the heat source, and therefore a gradation of austenite grain size within the reheated region was expected. Regions of bainite in the reheated microstructure were therefore searched for. Since bainite is known to exhibit lower fracture resistance than acicular ferrite the presence of such regions could be detrimental to the weld properties as a whole.

The austenite grain structure of the weld was investigated by etching polished specimens in saturated picric acid in methanol which contained an addition of wetting agent, namely sodium

di-octyl sulfosuccinate. The microstructural observations were carried out after repolishing and etching in 2% Nital. The use of this etching technique is after Frost *et al.* (1987). The etchant composition is given in Table 5.3.

The choice of alloys for this investigation was made in order to gain a comparison between the behaviour of a steel which gave a high volume fraction of acicular ferrite in the as-welded condition (alloy 113) with another which showed a smaller acicular ferrite fraction (alloy 114).

Composition	99ml Saturated Picric Acid in methanol 0.1% di octyl sulfosuccinate
Method	Etch in an ultrasonic bath for 2 minutes

Table 5.3 Details of the composition and treatment conditions of the picric acid based grain boundary etchant (after Frost *et al.* 1987)

5.4.4 Quantification of the Microstructure

Interpretation of the microstructure is far from trivial. It is impossible to rule out certain errors arising from the subjective nature of the process of interpretation. The ‘three dimensional’ appearance of SEM images produces variations in ‘grey level’ resulting from shadowing effects, making the use of image-analysis difficult. A process of tracing the acicular ferrite in the microstructure before image-analysis involves the same interpretation process as does point counting, and was found to be less readily applicable since tracing could not follow very fine features in the microstructure.

The volume fraction of acicular ferrite in each weld was determined by superimposing a rectangular grid of 378 points on the SEM micrograph, which gives a statistical error of around $\pm 5\%$ in measurement. Clearly plate-like regions appearing raised above the sample surface were interpreted as acicular ferrite and the inter-plate regions interpreted as martensite. The volume fraction of acicular ferrite was calculated using the expression

$$v_{\alpha_a} = \frac{N_{\alpha_a} + N_{\text{ind}}/2}{N_{\alpha'} + N_{\alpha_a} + N_{\text{ind}}}$$

where N_{α_a} and $N_{\alpha'}$ represents the number of points lying on regions of acicular ferrite and martensite respectively, with N_{ind} representing the number of indeterminate points. The points classed as indeterminate corresponded to regions of the microstructure that were difficult to interpret *e.g.* if a point fell on the boundary between an acicular ferrite plate and an inter-plate region, or when it was impossible to identify the microstructural component beneath the point. Half of such points were assumed to correspond to acicular ferrite.

5.5 Results

5.5.1 Microstructural Observations

The Effect of Variation of the Major Alloying Elements

Figures 5.4, 5.5 and 5.6 show the effect on the weld deposit microstructures of changes in the concentration of the major alloying elements. Figures 5.4 (a) and (b) show the essentially similar microstructures of alloys 112 and 113. Figure 5.5 (a) shows a high magnification image of alloy 112, with the microstructure of high carbon alloy 114 given in Figure 5.5 (b). The effect of manganese variation is shown by Figure 5.6 (a) and (b) which show the microstructures of alloys 115 and 116 respectively.

The Microstructural Effect of Chemical Segregation

Figure 5.7 (a) shows an example of the pronounced banding observed in the microstructure of alloy 114. Figure 5.7 (b) shows a solute depleted region of alloy 115 with a high fraction of acicular ferrite, markedly different from the microstructure shown in Figure 5.6 (a).

The Effect of Variation of Other Substitutional Solute Elements

Figure 5.8 (a) and (b) show the changes in weld microstructure as the nickel concentration is changed. Alloys 117 and 118 are respectively the high and low nickel variants of the series. Nickel has an intrinsic beneficial effect on the toughness of steel and this constitutes a major reason for its popularity in weld deposits. In body centered cubic iron, screw dislocations lying along $\langle 111 \rangle$ directions are dissociated in three dimensions on the three $\{11\bar{2}\}$ planes sharing the common $\langle 111 \rangle$ axis. The degree of dissociation is extremely small but is large enough to cause an increase in the flow stress with a consequent decrease in toughness. Nickel increases the stacking fault energy, thereby reducing the extent of dislocation dissociation, and hence makes plastic flow easier. The corresponding lowering of the ductile/brittle transition temperature is the major reason for the presence of nickel in high strength steels weld deposits.

Nickel does, of course, have other benefits *e.g.* it reduces the driving force for the transformation from austenite to ferrite (*i.e.* it is an austenite stabiliser) although its influence is not as pronounced as that of manganese.

The effect of increasing the molybdenum content of the weld deposit is shown in Figures 5.9 (a) and (b) which display the microstructures of alloy 119 and alloy 120, the high and low-molybdenum members of the alloy series respectively. Chromium variation effects are shown in Figure 5.10 (a) and (b), which show the respective microstructures of alloy 121 and 122.

5.5.2 Comparison of As-deposited and Reheated Microstructures

Figure 5.11 shows the change in the austenite grain morphology across the fusion boundary of the centre bead on the top layer. Figure 5.12 (a) and Figure 5.12 (b) show the microstructure

of the reaustenitised regions of alloy 113 and alloy 114 respectively. The equiaxed shapes of the reaustenitised grains are clearly evident.

5.5.3 Microhardness Testing

Figure 5.13 and 5.14 show the results of microhardness traverses across the fusion boundary between the centre bead of the top layer and a neighbouring underlying bead for alloys 113 and 114 respectively. Marked on the plots are the regions P1 and P2 corresponding to the columnar regions of the as-deposited microstructure. A layer of reaustenitised material separates these columnar grained regions.

Figures 5.15 and 5.16 show hardness traverse results across the fusion boundary into the reheated regions of alloy 119 and alloy 120 respectively. Figures 5.17 and 5.18 show hardness traverses across the fusion boundary of alloys 121 and 122. The microstructures of alloy 119 and alloy 121 in reaustenitised and tempered regions of the heat affect weld metal are shown in Figures 5.19 and 5.20 respectively.

5.5.4 Volume Fraction Measurements

The volume fraction of acicular ferrite in each alloy, as determined by point counting on high magnification micrographs is shown in Table 5.5. The data from Table 5.4 is presented graphically in Figure 5.21

5.6 Discussion

5.6.1 Microstructure of the Primary Weld Metal

Alloy 112 (Standard Alloy)

Figure 5.4 (a) illustrates all the essential features of the structure of a prototype high strength steel weld. It consists of fine acicular ferrite and martensite mixture with the volume fraction of acicular ferrite being very large. The columnar austenite grains are clearly visible and are free from phases such as allotriomorphic ferrite or Widmanstätten ferrite. The acicular ferrite plates show some size variation, although this could be a stereological effect. The uniformity of the microstructure is remarkable as is the number density of acicular ferrite plates. None of the plates have developed to any appreciable length because the nucleation sites are so closely spaced that physical impingement with other plates occurs soon after the plates become large enough to be visible. The low magnification image shows evidence of a small amount of chemical segregation, although this does not seem to have a profound effect on the microstructure, presumably because the kinetics of transformation are in any case quite rapid. In welds it is the substitutional alloying element segregation which leads to the major microstructural effects – ferrite forms in regions depleted of austenite-stabilising elements and

Alloy	Acicular Ferrite Fraction ± 0.5
A112	0.75
A113	0.78
A114	0.43
A115	0.53
A116	0.76
A117	0.53
A118	0.78
A119	0.54
A120	0.75
A121	0.58
A122	0.66

Table 5.5 Volume fraction measurements of acicular ferrite in the primary weld metal region of a variety of weld deposits. The measurements were in each case made for the centre bead in the top layer. The balance of the microstructure is martensite.

the carbon partitioned from the ferrite produces bands of carbon-enriched martensite. Thus the low carbon content of the alloys used here minimises any consequences of substitutional solute segregation.

Alloy 113 (Low Carbon)

This alloy was intended to be a lower carbon version of alloy 112, but it was difficult in practice to achieve a large reduction because of the raw material used in electrode manufacture. Hence its chemical composition is only slightly different from alloy 112. This fact is reflected in a very similar microstructure, as shown in Figure 5.4 (b). As expected, the effects of chemical segregation are less obvious again in alloy 113, presumably because of the somewhat smaller carbon content of the alloy. The volume fraction of acicular ferrite is found to be large.

Alloy 114 (High Carbon)

The effect of increasing the carbon content of the weld deposit is shown by comparing the high magnification image of alloy 112 in Figure 5.5 (a) with the high magnification image of alloy 114 in Figure 5.5 (b). Alloy 114 represents a significantly higher carbon variant (0.079 wt%), and its microstructure reflects this. The high magnification image reveals significantly larger quantities of martensite and a correspondingly lower fraction of acicular ferrite. The acicular

ferrite plate shapes are much more prominent since their development has been influenced to a lesser degree by impingement with other plates nucleated on adjacent inclusions. Indeed there is a clear tendency for acicular ferrite *sheaves* to develop probably because the nucleation rate on inclusions has been reduced by the higher carbon content. A further consequence of the increased carbon content is that bands containing large amount of martensite can be observed frequently (*e.g.* Fig. 5.7 (a)). This results from substitutional solute segregation whose very prominent effect on the microstructure is exaggerated by the partitioning of large amounts of carbon in to the solute-depleted regions, as can clearly be seen in the low magnification image of alloy 114 shown in Figure 5.7 (a).

It should be noted that although the carbon concentration of 0.079 wt% is not much greater than the 0.062 wt% of alloy 112, the development of the microstructure is very sensitive to carbon variations at low carbon concentrations. This is because the mean carbon concentration approaches the solubility of carbon in ferrite.

Manganese Variation

Figure 5.6 (a) shows the microstructure of the high manganese alloy 115. An increase in the manganese concentration (*c.f.* alloys 112, 115) seems to have a similar effect to the increase in carbon, giving a large amount of martensite in the microstructure. The tendency for forming sheaves of acicular ferrite seems to be somewhat lower than for the high carbon variant. Thus it would appear advantageous from the point of view of mechanical properties to achieve high strength via manganese alloying rather than by an increase in the carbon concentration.

A reduction in the manganese concentration in alloy 116, shown in Figure 5.6 (b) leads to the expected microstructure containing almost exclusively acicular ferrite, whose morphology is similar to that of alloy 112. Allotriomorphic ferrite and Widmanstätten ferrite are found to be absent despite the lower manganese concentration. It is apparent from comparing alloys 112, 114, 115 and 116 that the higher alloy content alloy 114 and 115 have finer acicular ferrite plate sizes, despite the fact that the nucleation rate of these alloys is lower than for alloys 112 and 116. It is likely therefore that the fine size of the acicular ferrite plates is a result of the temperature of formation rather than impingement effects. For bainite, apparent plate thickness has been consistently reported to increase as the transformation temperature increases (Bhadeshia, 1982b; Pickering, 1958; Ohmori, Ohtani & Kunitake, 1971).

The Effect of Chemical Segregation on Microstructure

Solute segregation between the solidifying weld metal and the liquid is assumed to be the cause of the clear banding in the microstructure of the high carbon alloy 114 (Fig. 5.7 (a)). This banding is made more pronounced by the large difference in the amount of martensite

in the microstructure. It appears that the microstructure of the alloy is very sensitive to the substitutional alloy content in this high carbon variant of the series.

In the high manganese alloy 115, a high magnification micrograph from a solute depleted region of alloy 115, is shown in Figure 5.7 (b). Comparing this image with that of the bulk of material within the primary weld metal it can be seen that the effects of long range chemical segregation have a profound effect on the microstructure. A decrease in the substitutional solute content increases the driving force for ferrite formation, thus increasing the transformation rate. It appears that the resultant microstructure is sensitive to the solute content, but to a lesser extent than is seen in alloy 114, since the carbon level of the alloy is smaller.

Nickel Variation

A large nickel concentration (Fig. 5.8 (a)) increases the martensite fraction in the microstructure, whereas a reduction (alloy 118, Fig. 5.8(b)) below the concentration in alloy 112 does not have much of an effect. The lack of change on lowering the nickel concentration is because the difference made to the transformation kinetics between alloys 112 and 118 is not large. Nickel also has a large partition coefficient with liquid iron and consequently has a greater tendency to segregate (Gretoft *et al.* 1986). Thus bands of martensite are apparent in the low magnification image of alloy 117.

Molybdenum and Chromium Variations

The effects of both molybdenum and chromium on the primary microstructure are as expected; an increase in the concentration of each element relative to alloy 112 leads to an increase in the martensite volume fraction, and vice versa. This effect is shown in Figures 5.9 and 5.10 which display the microstructures of the high molybdenum, low molybdenum, high chromium and low chromium variants respectively. Apart from the effect on the fraction of acicular ferrite, as will be discussed later, the major effect manifests itself in the multi-pass deposits where the secondary hardening tendency of Mo and Cr assumes significance.

5.6.2 Comparison of As-Deposited and Reheated Microstructure

A significant difference in the γ grain morphology across the fusion boundary can be seen in Figure 5.11 which shows the austenite grain structure of alloy 113. The grain structure is revealed by using saturated picric acid in methanol with a small addition of sodium di-octyl sulfosuccinate as an etchant. As can be seen from Figure 5.12 (a) the microstructure of Alloy 113 is very similar in the columnar grained region and in the equiaxed region of the multi-pass weld. Figure 5.12 (b) show that this is also the case for alloy 114. The finer grain size of the equiaxed region has resulted in a slightly greater proportion of bainite, but the effect of cooling reaustenitised material at a different the cooling rate in the reheated regions has not increased

the tendency to form other grain-boundary nucleated phases such as allotriomorphic ferrite and Widmanstätten ferrite.

5.6.3 Hardness Traverses

Figures 5.13 and 5.14 show that the variation of hardness across the fusion boundary of alloy 113 and alloy 114 is small, in comparison with the variations in hardness that arise from statistical errors and the local variation in the microstructure of the welds. In combination with the micrographs of the structure in the columnar and reheated regions, the hardness traverses emphasise the mechanical and microstructural homogeneity of the welds. The results indicate the achievement of the goals of the designers in producing a weldment composition that would maximise the tendency to reaustenitise the reheated regions, while ensuring that these regions transformed to a structure similar to that of the as-deposited regions after the passing of the arc.

Comparison of the hardness traverses across fusion boundaries in alloy 119, 120, 121 and 122, given in Figures 5.15, 5.16, 5.17 and 5.18 respectively, show that there is little change in hardness between the as-deposited, reaustenitised and tempered regions. This observation is particularly significant for the welds that have a high concentration of elements which promote secondary hardening. The variation of the hardness is small compared to the general scatter in microhardness measurements. It is likely that the small carbon content of the alloys makes the precipitation of carbides unlikely within the time scale of the reheating process. The significance of the absence of secondary hardening effects is that the mechanical homogeneity of the weld is not affected adversely by the choice of the alloy chemistry.

The microstructure changes associated with the hardness traverses in alloy 119 and alloy 121 are illustrated in Figure 5.19 and Figure 5.20 respectively. In each case micrograph (a) represents the microstructure of the central reaustenitised region, with micrograph (b) illustrating the microstructure of near the final indent of the hardness traverse, in the columnar region of a tempered bead.

5.6.4 Volume Fraction Measurements

The volume fraction measurements of acicular ferrite listed in Table 5.5 show the expected general trend that the more highly alloyed steels should display a higher volume fraction of martensite than the lightly alloyed variants of the series. These data are displayed graphically in Figure 5.21.

5.7 Conclusions

From the microstructural observations it can be concluded that the the most potent factor in determining the extent of transformation to acicular ferrite in weld deposits that do not

form any allotriomorphic ferrite or Widmanstätten ferrite is the carbon concentration of the alloy. The presence of austenite stabilising substitutional solutes (*e.g.* Mn and Ni) also inhibits the formation of acicular ferrite. The marked effect of solute segregation in the high carbon alloy 114 indicated how much more sensitive the microstructure of the weld deposit is to the substitutional alloy content when the level of carbon is raised.

In the manganese or nickel-rich weld deposits, regions can be found in the weld that have significantly higher acicular ferrite fractions than the bulk of the deposit. The scale of these variations is larger than the banding observed in alloy 114, but is presumably a consequence of substitutional alloy partitioning. It is noteworthy that the large difference in microstructure between alloy 113 and alloy 115 is essentially achieved by a change in the manganese content of 0.5 wt%. So sensitive is the microstructure to alloy composition that substitutional element partitioning during solidification need not be dramatic in order to achieve significant changes in microstructure.

In the alloys where the amount of acicular ferrite is small, it is common to see a clustering of ferrite plates in sheaf structures rather than the more classic structures desired in welds. The lower nucleation rate of the more highly alloyed steels makes nucleation on inclusions less rapid and therefore autocatalytic effects become more important *i.e.* acicular ferrite plates have the opportunity to nucleate on previously formed plates before hard impingement with neighbouring sites makes this impossible. It is also significant that there is a clear size difference in the plates of the highly alloyed steels compared to those in the more lightly alloyed variants of the series. This is a result of the different temperatures at which the bulk of transformation occurs during the cooling of the weld; the reaction start temperature depends on the alloy chemistry.

The microstructural homogeneity of the multi-pass welds studied is found to be remarkable. Austenite grain boundaries appear free of allotriomorphic ferrite and Widmanstätten ferrite except for isolated regions in some leaner alloys. The effect of chemical segregation, however, does cause second order variations in the microstructure. In the high carbon alloy the variation of the microstructure due to segregation occurs within individual columnar grains. In the high manganese alloy solute depleted regions can be found where whole columnar grains appear to show a much higher acicular ferrite fraction than in the bulk alloy.

Hardness traverses across the fusion boundaries of alloys in the series reveal no observable trends in the properties of the deposit resulting from effects such as tempering and the difference in austenite grain size. In steels in which the concentration of secondary hardening elements is high, there is no evidence of a marked increase in the hardness of the tempered regions. This fact is interpreted as indicating that the low carbon content of the alloys prevents significant precipitation of the alloy carbides that cause secondary hardening.

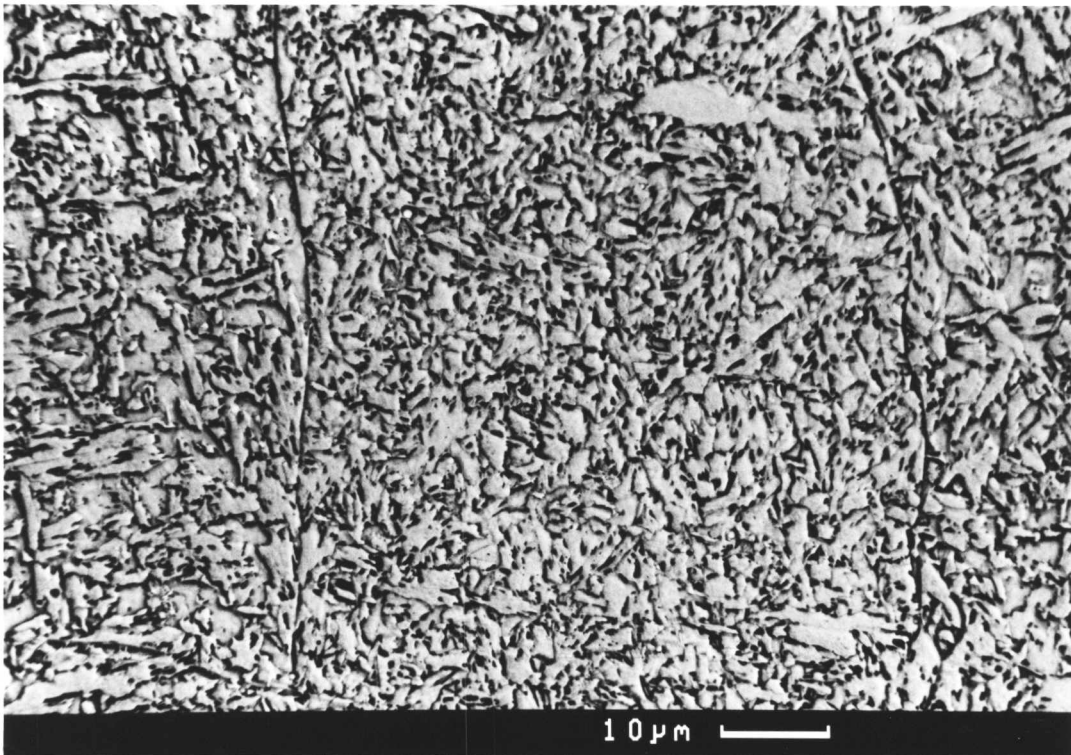
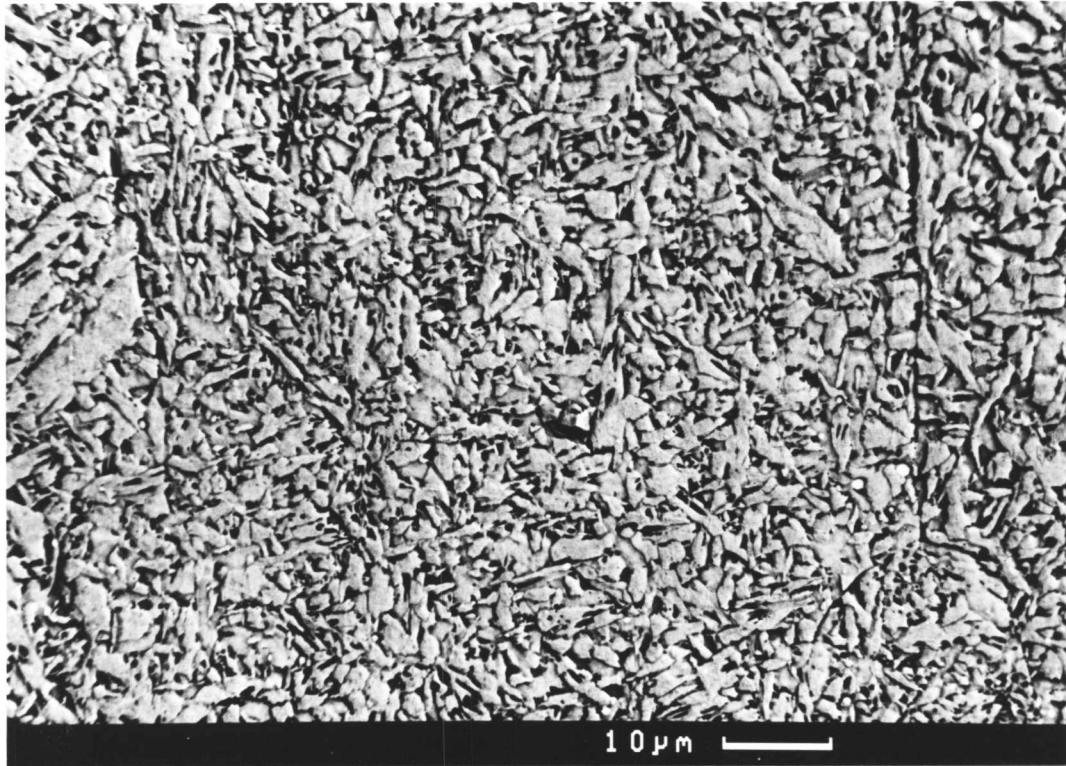


Figure 5.4 a) The microstructure of alloy 112 (standard alloy) which shows the essential characteristics of high strength steel weld deposits. A finer grained region of possible solute enrichment due to segregation is arrowed. b) The microstructure of alloy 113, essentially similar to that of alloy 112.

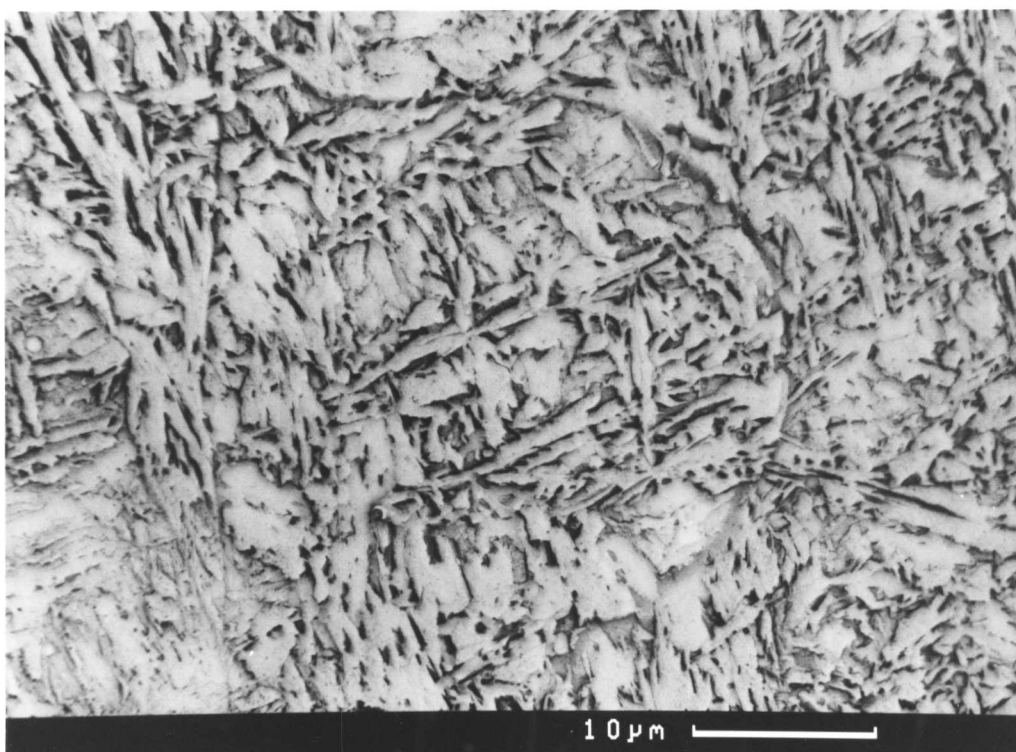
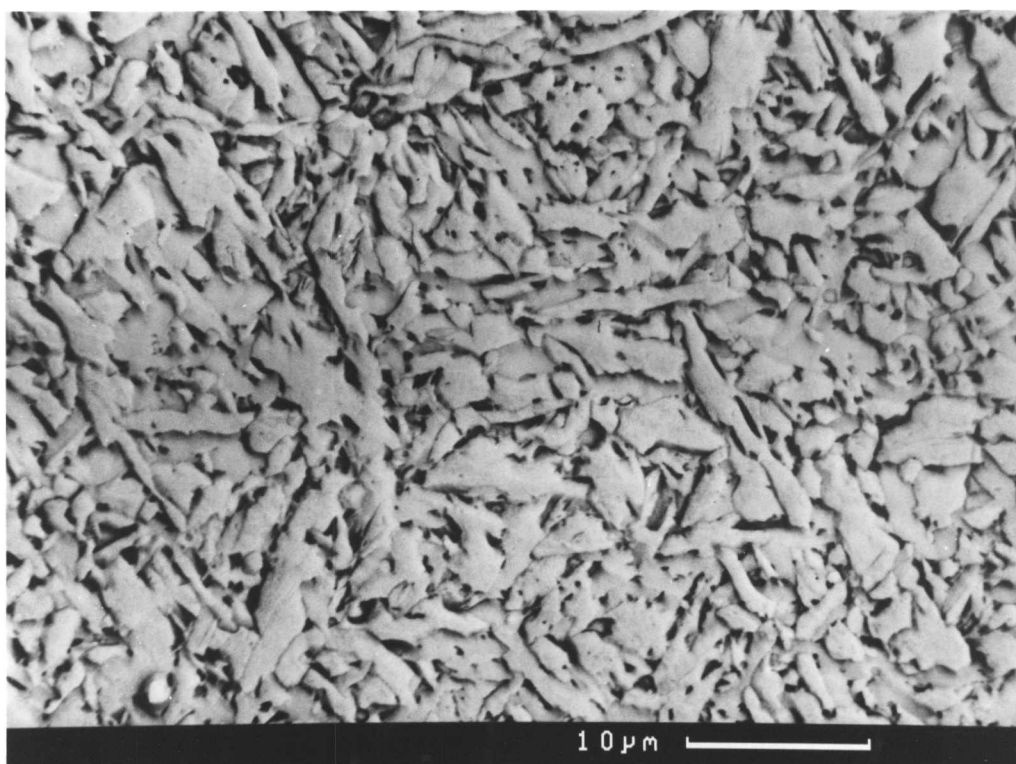


Figure 5.5 a) A high magnification image of the microstructure of alloy 112.
b) The microstructure of alloy 114, the high carbon variant of the alloy series.
Both micrographs are of the centre bead on the top layer of the weld.

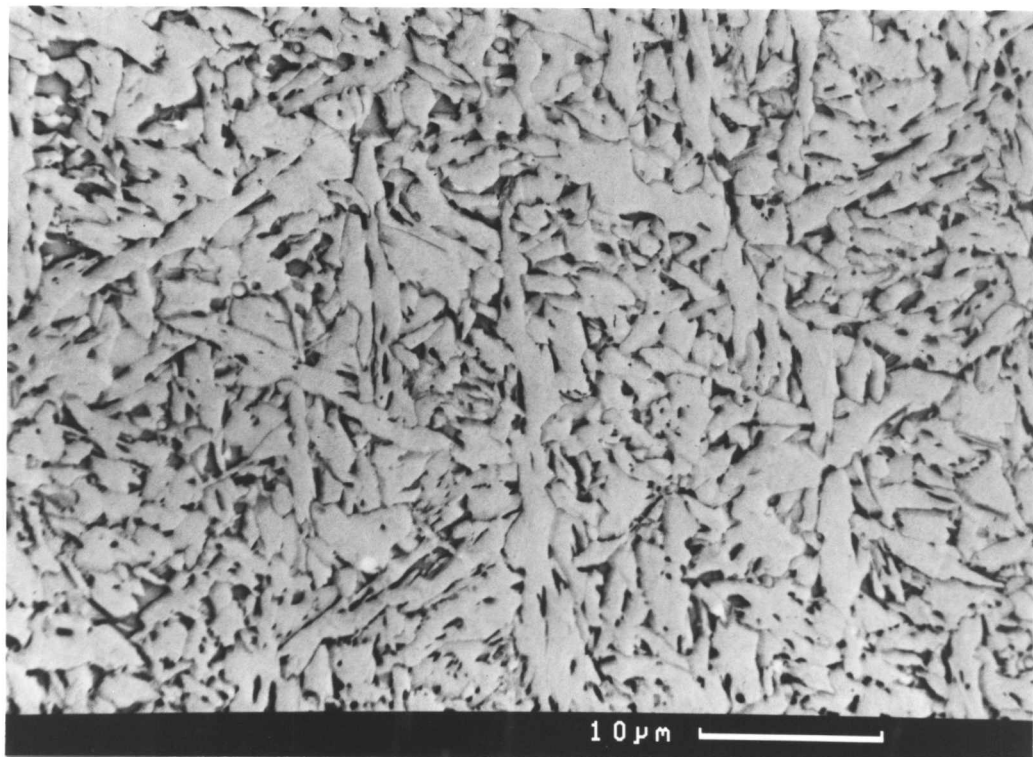
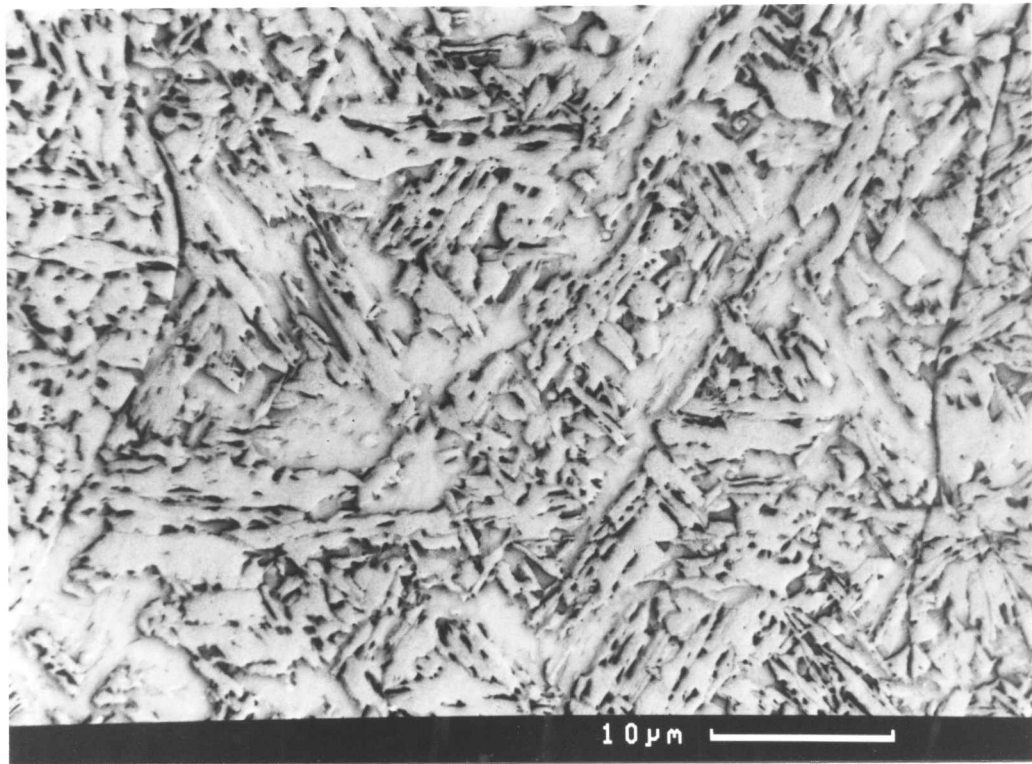


Figure 5.6 a) The microstructure of the high manganese weld deposit, alloy 115. b) The microstructure of alloy 116, low manganese variant of the alloy series. Both micrographs are of the centre bead on the top layer of the weld.

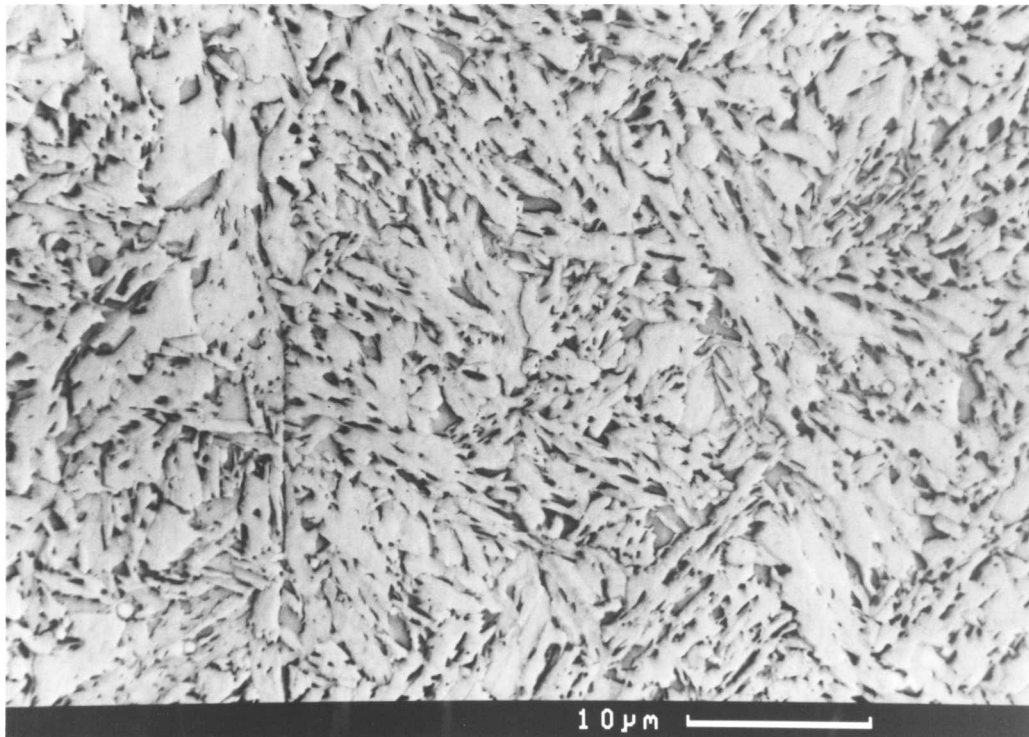
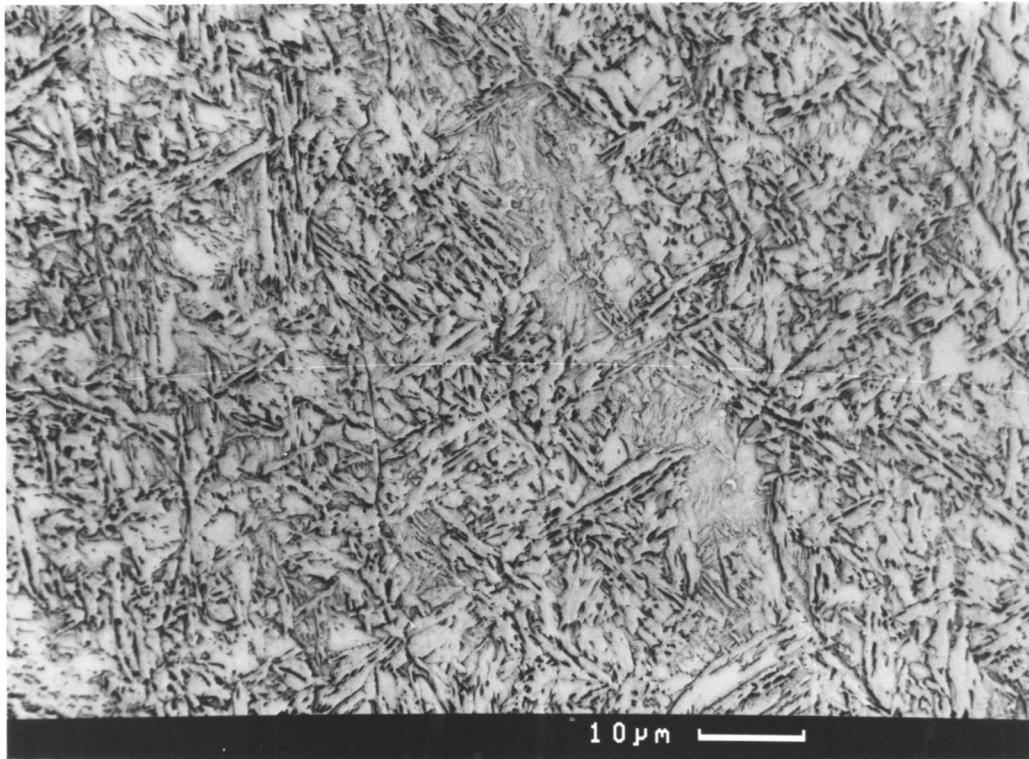


Figure 5.7 a) A micrograph of as-deposited alloy 114 showing the pronounced banding in the microstructure resulting from solute segregation. b) A micrograph of a solute depleted region in as-deposited alloy 115, showing a large fraction of acicular ferrite.

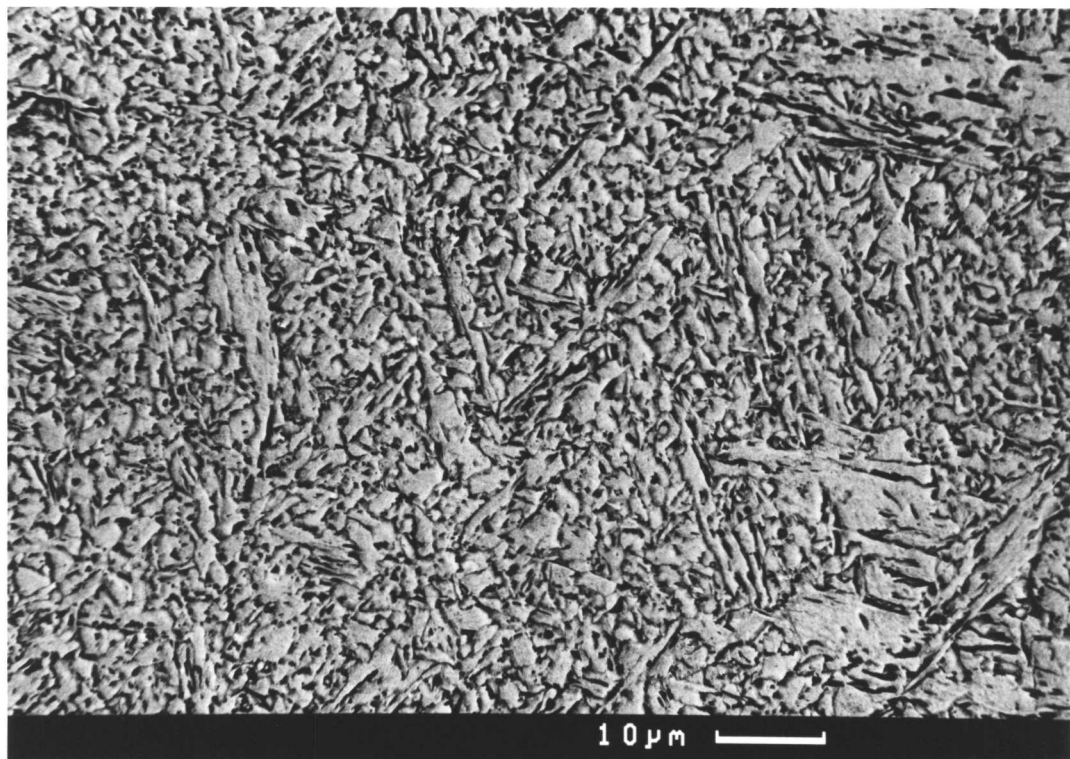
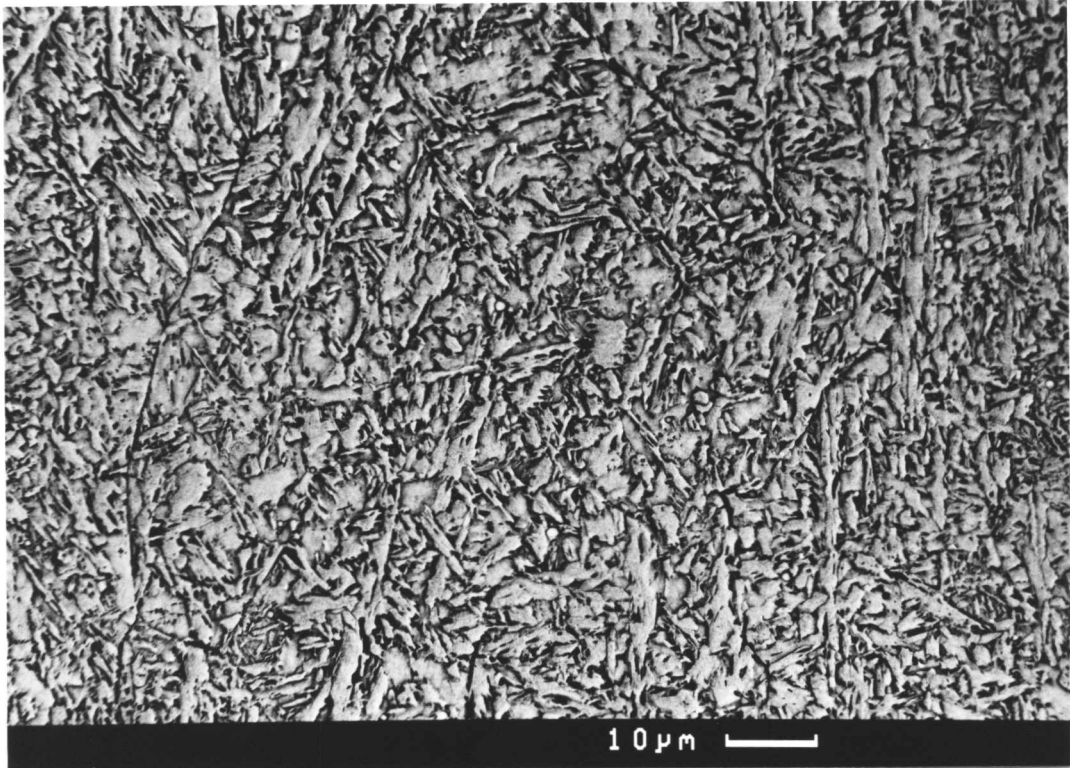


Figure 5.8 a) The as-deposited microstructure of alloy 117, the high nickel member of the alloy series, with region of high martensite content arrowed. b) The as-deposited microstructure of the low nickel variant, alloy 118.

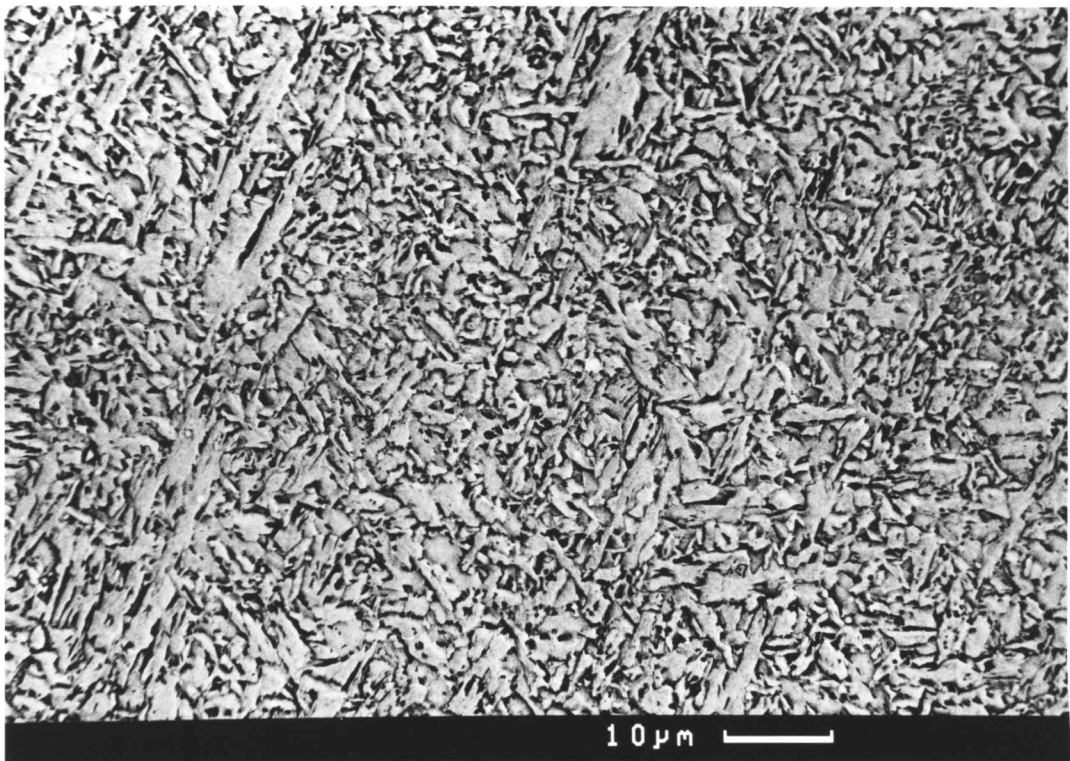
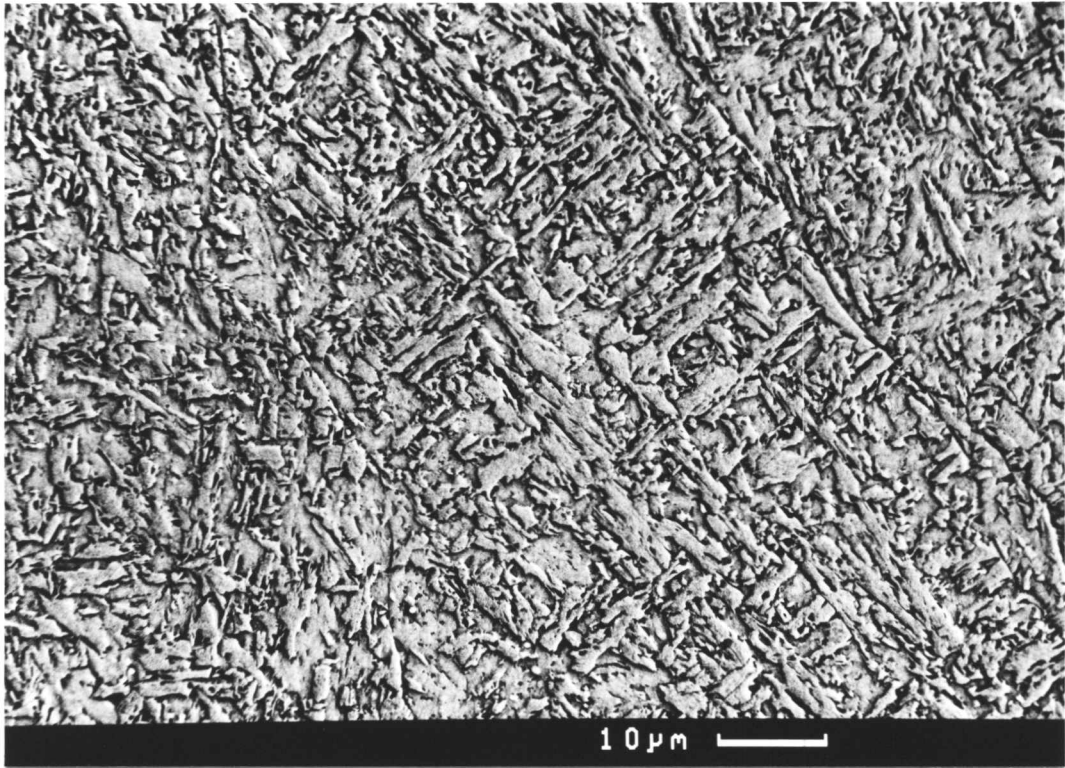


Figure 5.9 a) The as-deposited microstructure of alloy 119, the high molybdenum member of the alloy series. b) The as-deposited microstructure of low-molybdenum alloy 120.

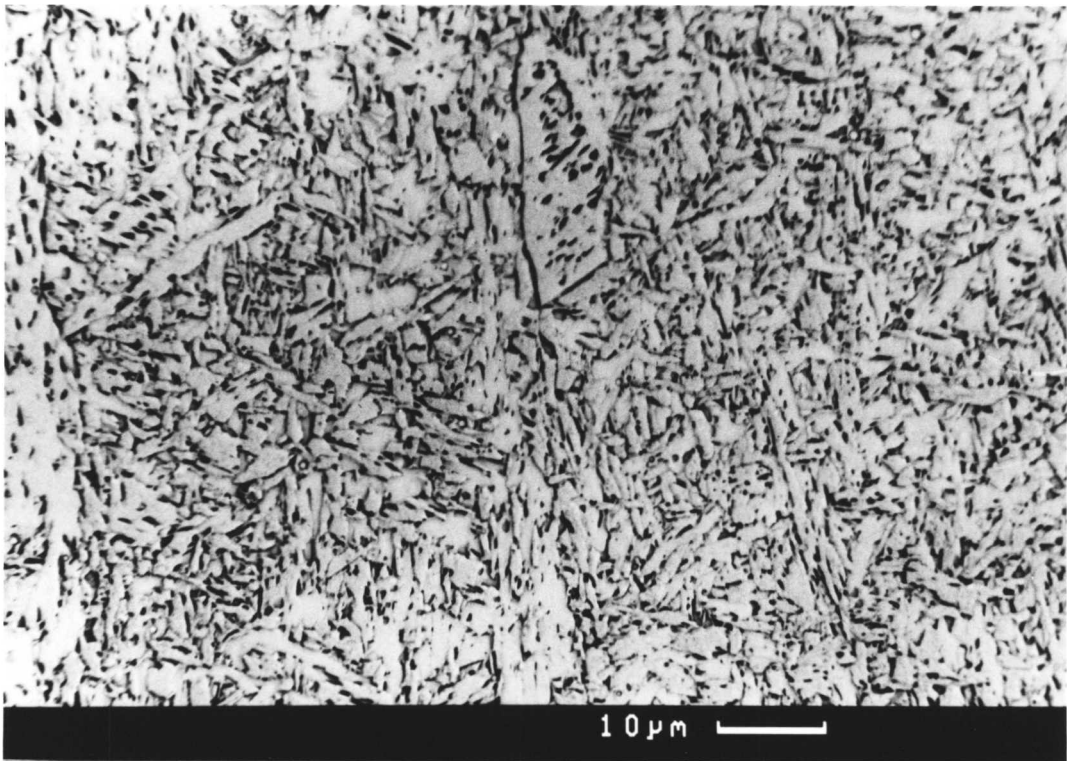
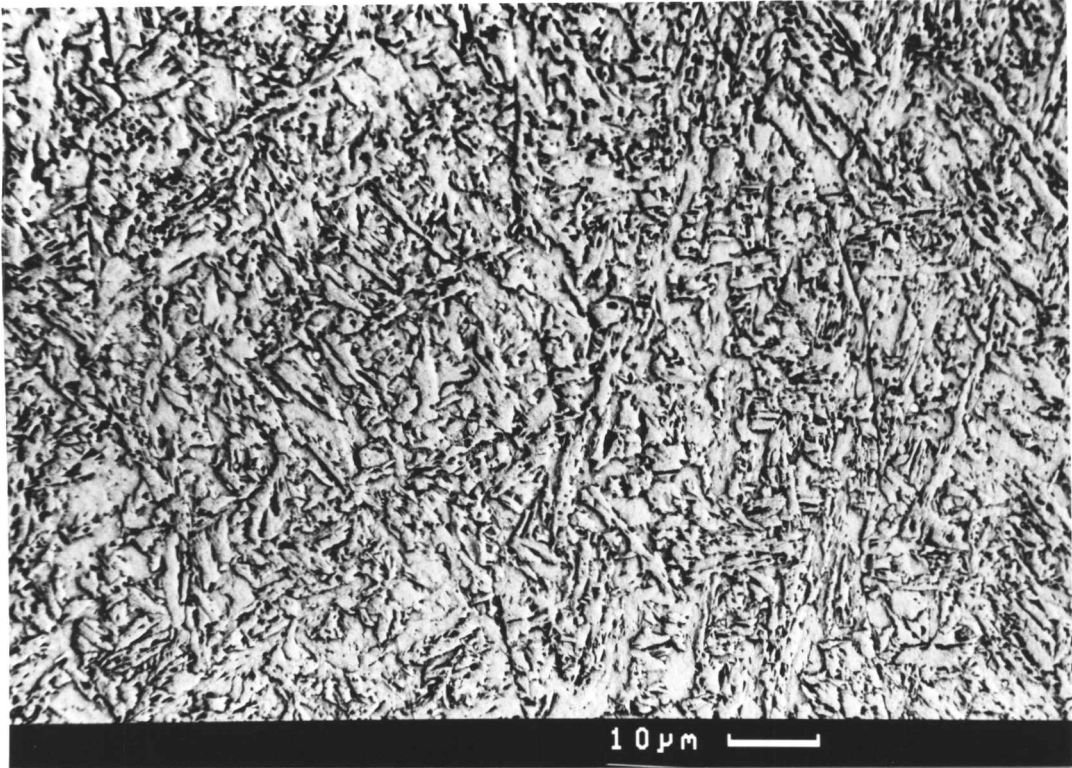


Figure 5.10 a) The as-deposited microstructure of high-chromium alloy 121.
b) The as-deposited microstructure of the low chromium alloy 122.

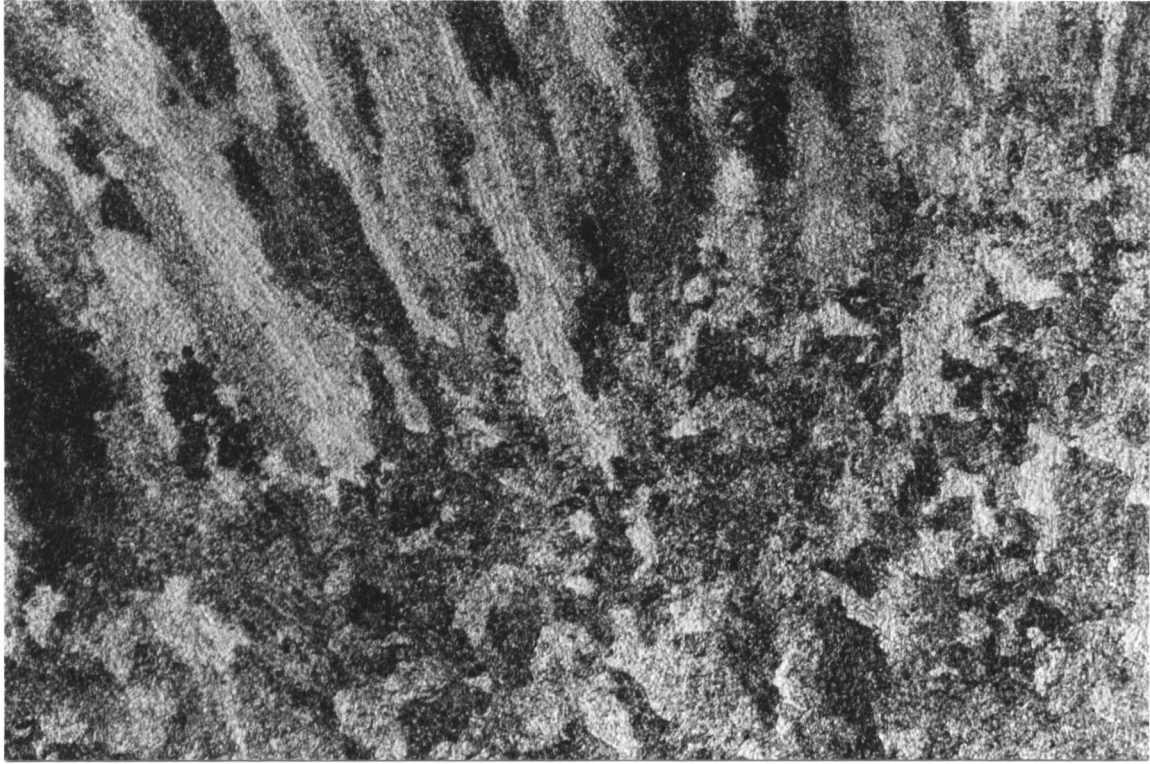


Figure 5.11 The outline of prior austenite grains across the boundary between the as-deposited and the reheated regions in alloy 113.

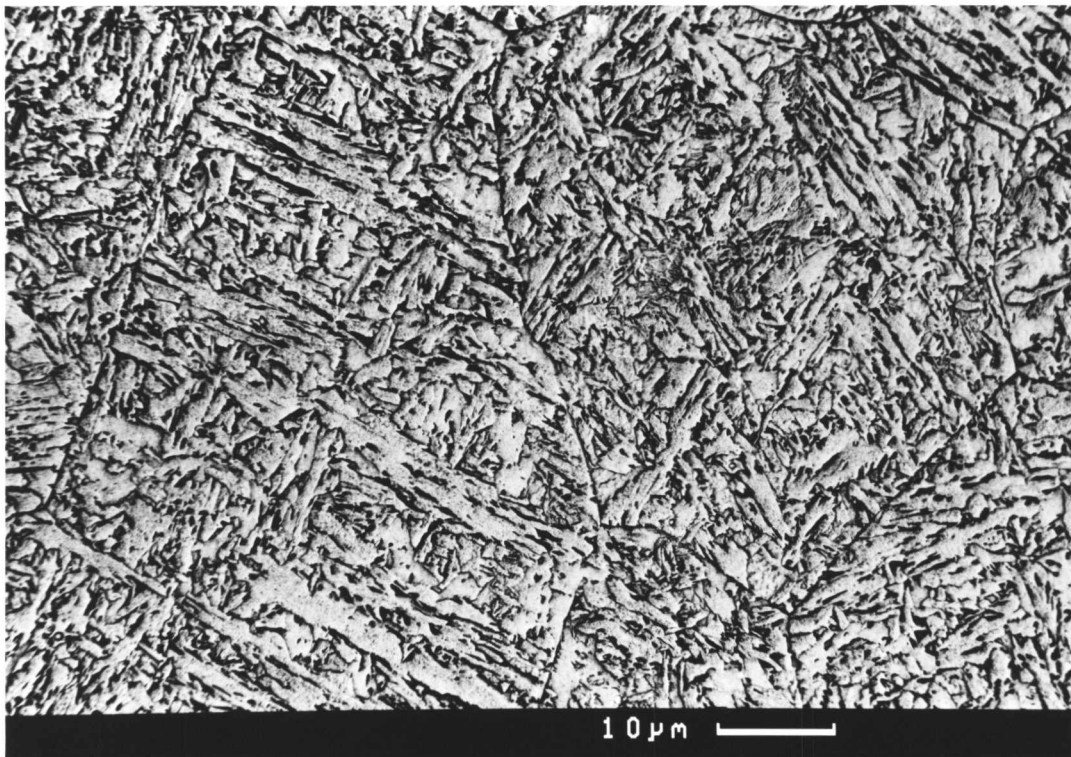
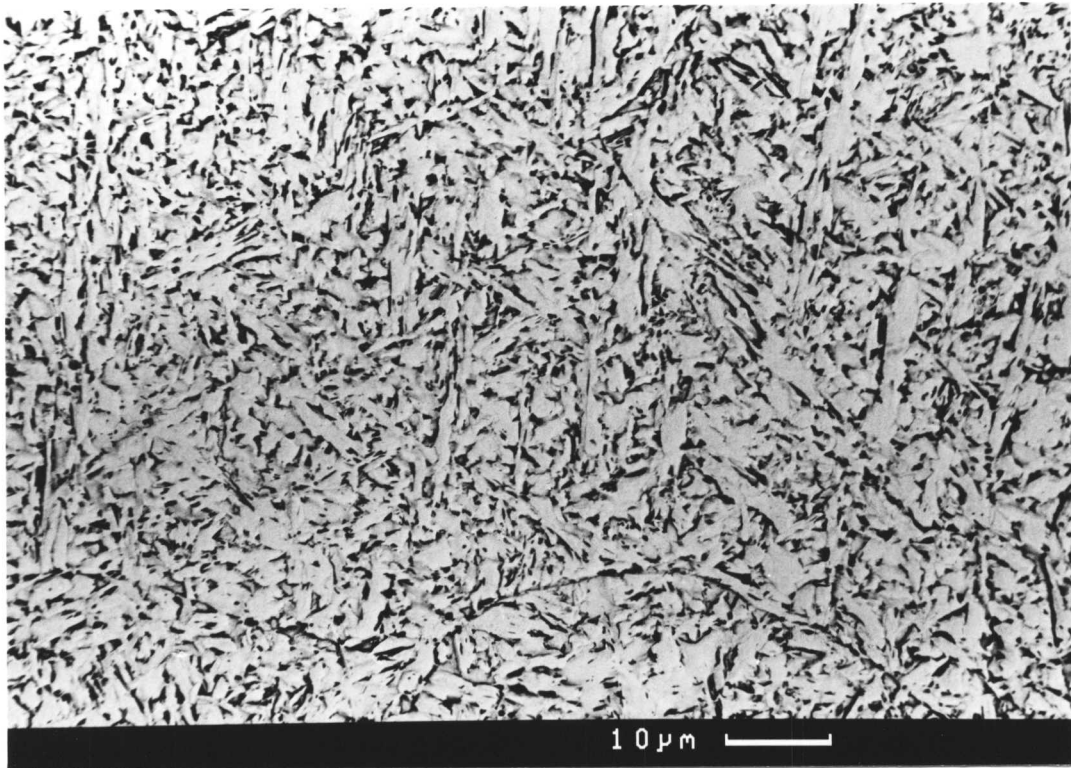


Figure 5.12 a) A micrograph of the re-austenitized metal of alloy 113 in the heat affected region of a previously deposited bead. b) A micrograph of the re-austenitized material in the heat affected region of alloy 114.

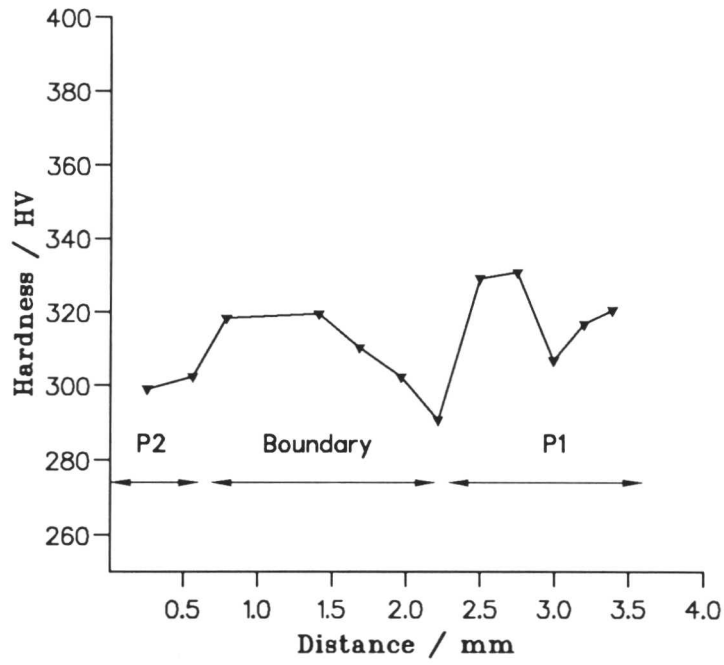


Figure 5.13 Hardness traverse across the fusion boundary in alloy 113.

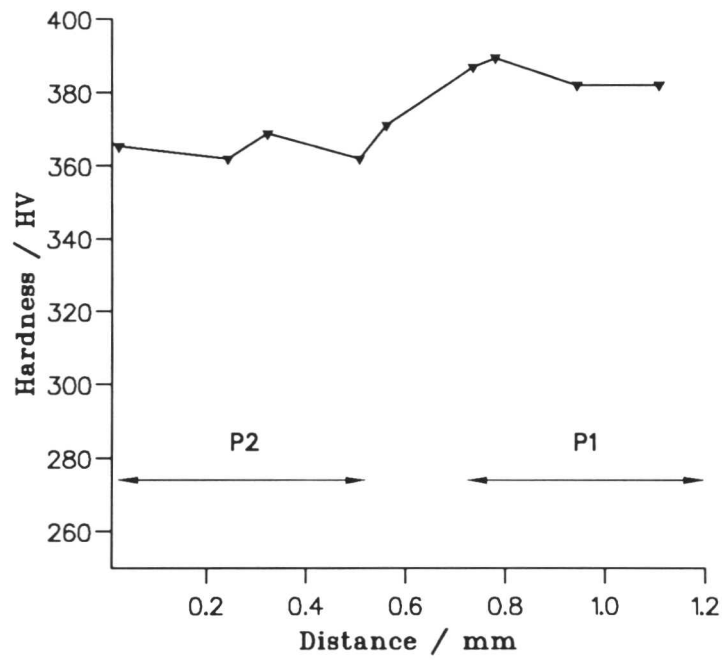


Figure 5.14 Hardness traverse across the fusion boundary in alloy 114.

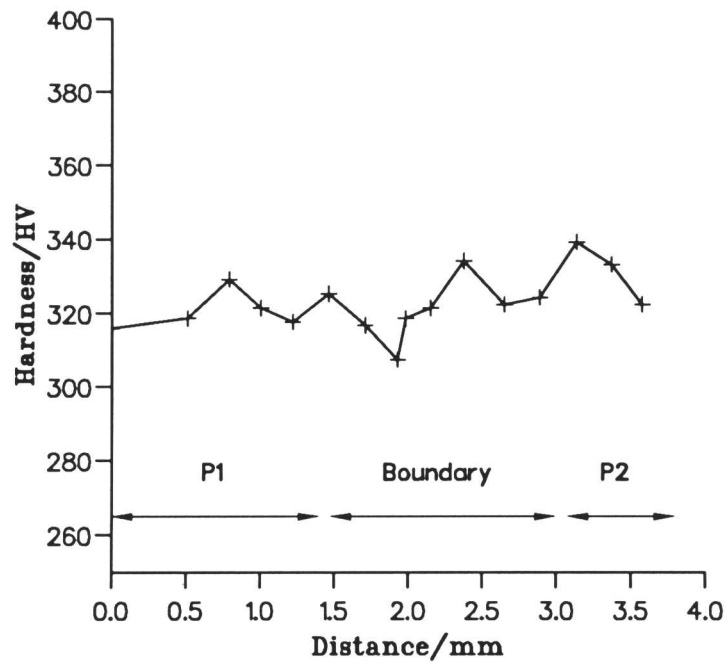


Figure 5.15 Hardness traverse across the fusion boundary in alloy 119, the high molybdenum variant of the alloy series.

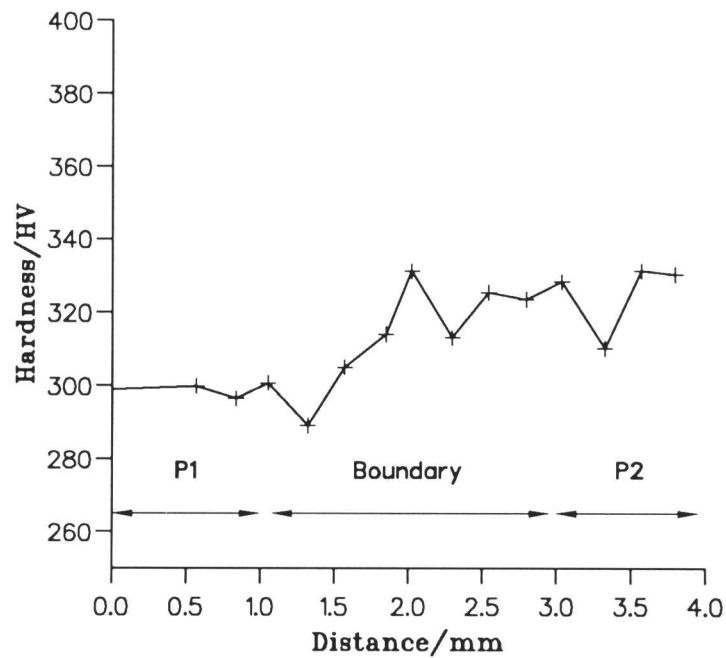


Figure 5.16 Hardness traverse across the fusion boundary in alloy 120, the low molybdenum variant of the alloy series.

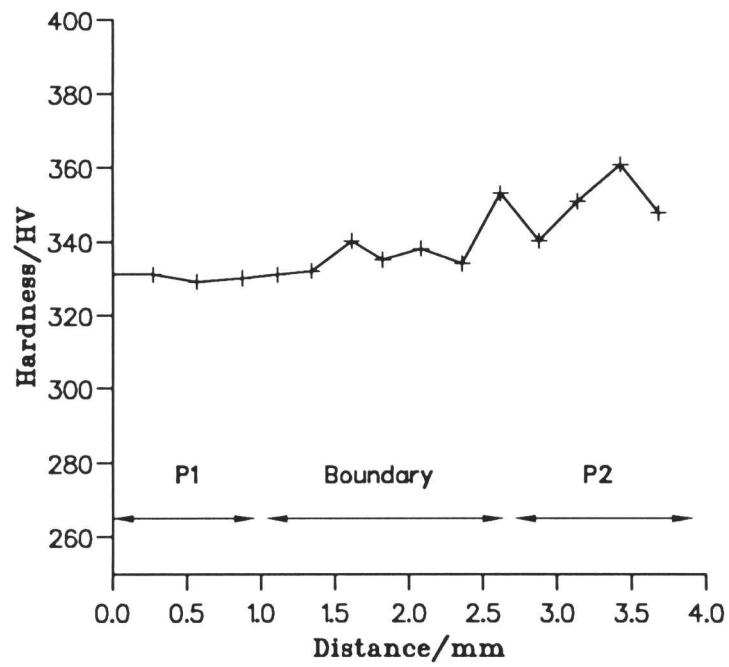


Figure 5.17 Hardness traverse across the fusion boundary in alloy 121, the high Chromium variant of the alloy series.

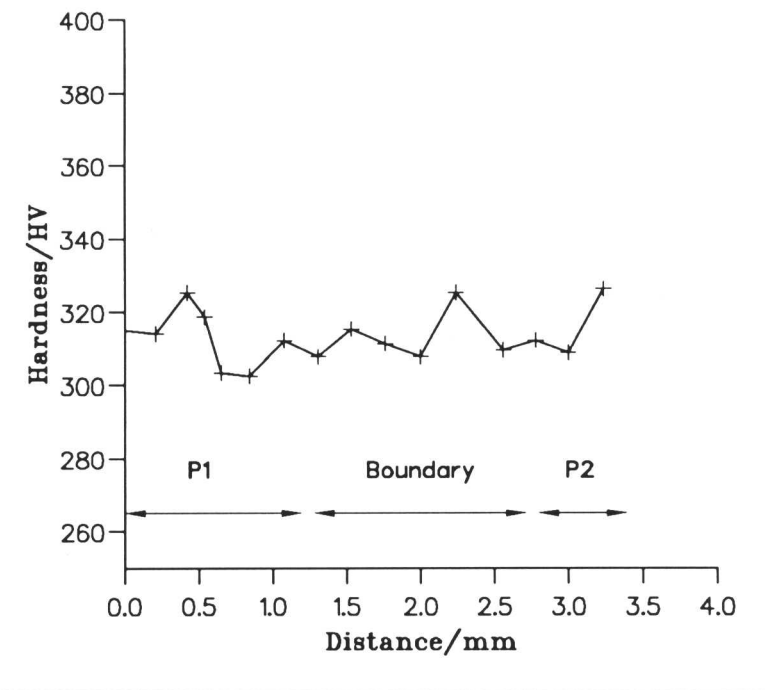


Figure 5.18 Hardness traverse across the fusion boundary in alloy 122, the low Chromium variant of the alloy series.

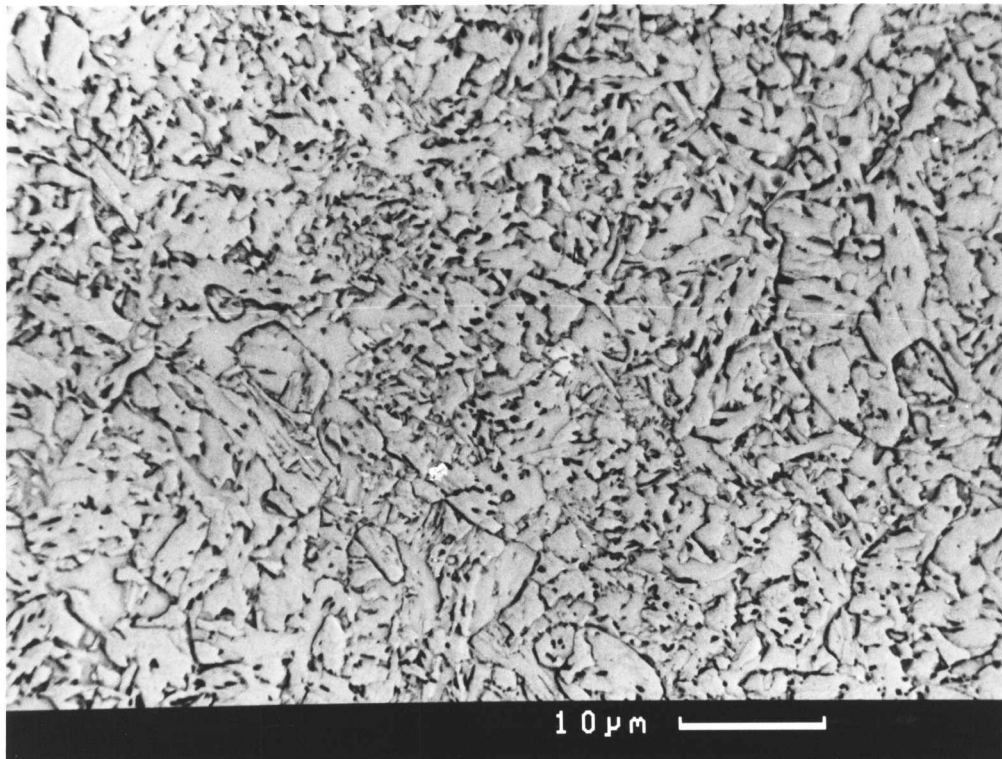
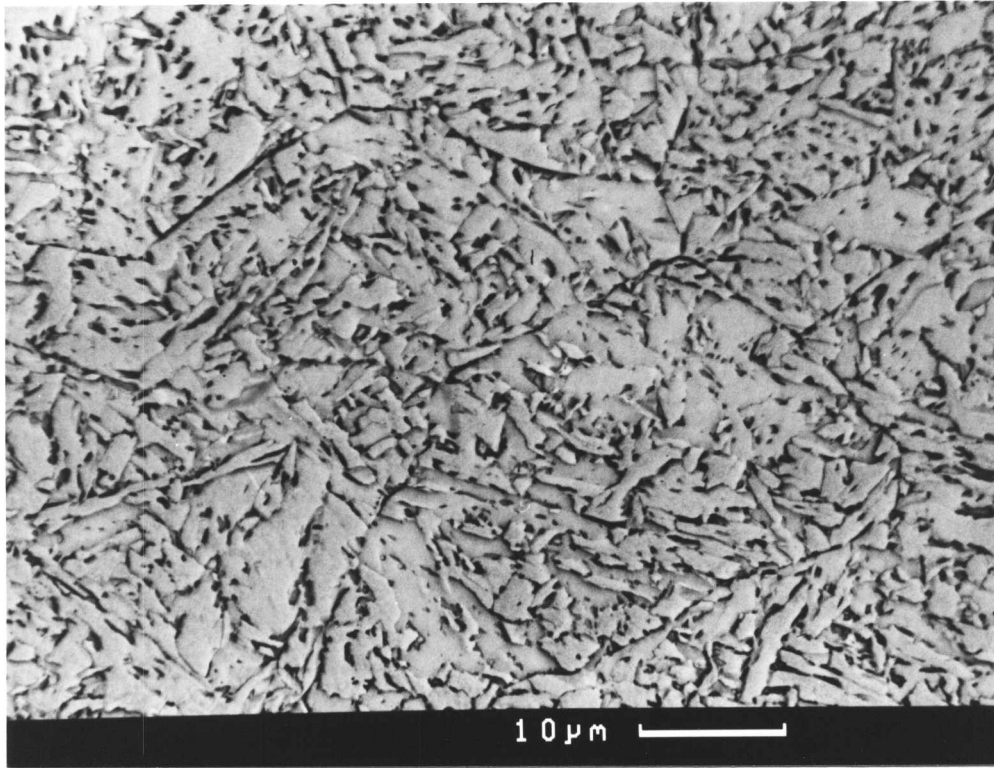


Figure 5.19 a) The microstructure of high-temperature re-austenitised weld metal in alloy 119. b) Microstructure of the columnar region of tempered weld metal in alloy 119.

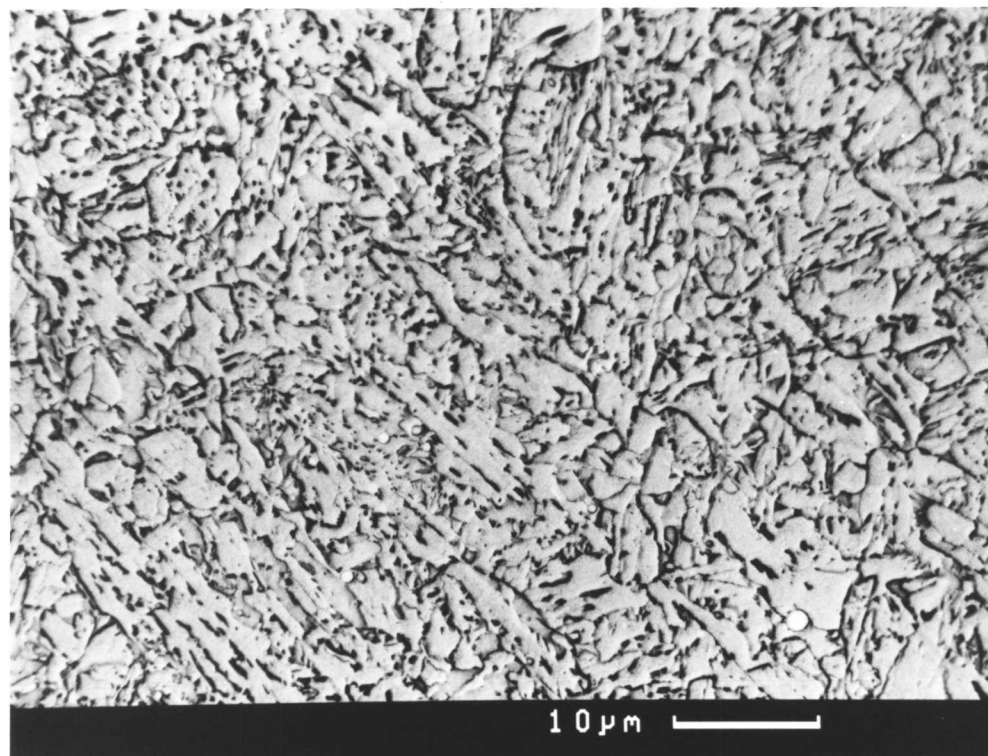
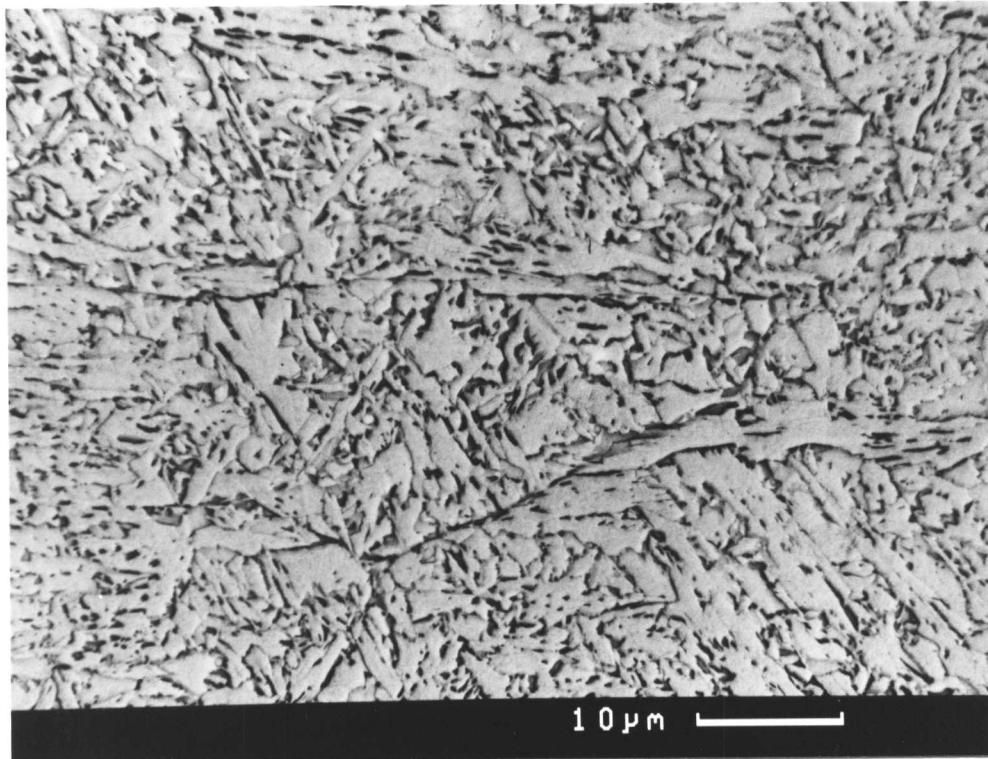


Figure 5.20 a) The microstructure of high-temperature re-austenitised weld metal in alloy 121. b) Microstructure of the columnar region of tempered weld metal in alloy 121.

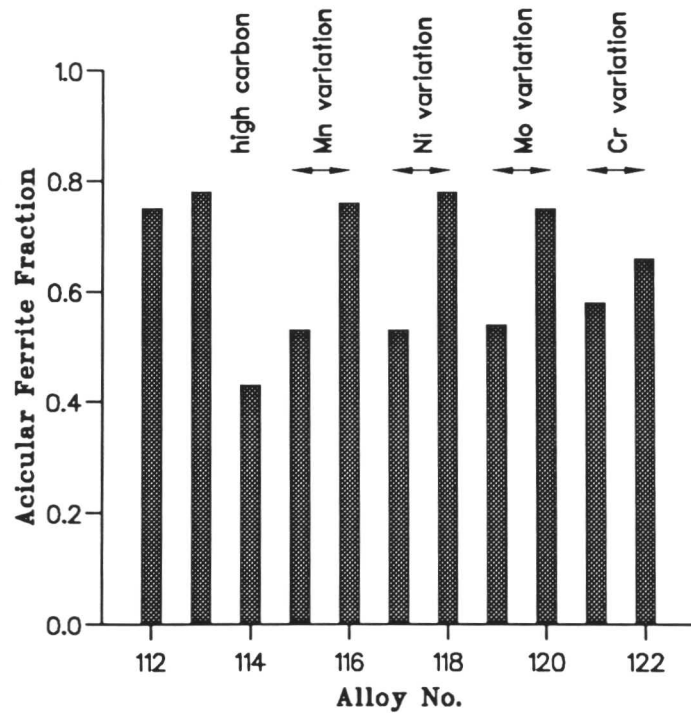


Figure 5.21 A graphical presentation of the measured acicular ferrite fractions in the as-deposited regions of the experimental weld series.

CHAPTER 6

Modelling the Microstructure and Properties of High Strength Steel Welds

6.1 Introduction

Following characterisation of the microstructure of a series of experimental high strength steel welds provided by ESAB, an attempt is made here to predict the microstructure from a knowledge of the chemical composition and thermal history of each weld alone. An attempt is also made to predict some mechanical properties from knowledge of the weld microstructure.

Existing models for the strength of welds (*e.g.* Sugden & Bhadeshia, 1988) are inadequate when applied to the type of weld considered here since the models group acicular ferrite and microphases together as one microstructural component. In microstructures consisting of substantial fractions of acicular ferrite and martensite it is necessary to account for the effect of these two phases separately. We begin with the methodology for estimating the microstructure, which is then related to the mechanical properties.

6.2 Previous Work

The weld microstructure model developed by Bhadeshia and co-workers is based on the following procedure:

- (a) From knowledge of the chemical composition of the weld, the composition of the solute-depleted regions of the weld is estimated (Gretoft *et al*, 1986).
- (b) Thermodynamic methods are used to estimate transformation temperatures such as M_S , B_S and Ae'_3 (Bhadeshia 1981a, 1981b, 1981c; Shiflet *et al*, 1978).
- (c) The theory for TTT-curve prediction (Bhadeshia, 1982a) is used to estimate the isothermal transformation diagram for the solute depleted regions of the weld. The start temperature for the allotriomorphic ferrite reaction is estimated using the Scheil approximation.
- (d) The start temperature for Widmanstätten ferrite is obtained by calculating the cross-over point of the predicted upper and lower C-curves (Bhadeshia *et al*, 1985).
- (e) Between the upper and lower limits set as its transformation temperature range allotriomorphic ferrite is assumed to grow by a paraequilibrium mechanism consistent with the diffusion of carbon in the austenite ahead of the interface (Bhadeshia *et al*, 1985).
- (f) Between its calculated start time and an empirically-set limiting time for impingement with intragranularly nucleated phases, Widmanstätten ferrite is assumed to grow with kinetics estimated by the Trivedi theory for plate lengthening (Trivedi & Pound, 1969).
- (g) The calculated volume fractions of the determined phases are subtracted from unity, giving the acicular ferrite fraction determined by difference (Bhadeshia *et al*, 1985). Note that the calculated acicular ferrite content therefore includes any microphases.

6.3 Application of the Bainite Kinetics Model to the Acicular Ferrite Reaction

6.3.1 The Connection Between Bainite and Acicular Ferrite

It has been argued by Yang and Bhadeshia (1987) that acicular ferrite and bainite are in fact identical in transformation mechanism, the morphological difference between them arising during nucleation. Bainite does so on austenite grain boundaries, whereas acicular ferrite nucleates on the non-metallic inclusions present inside the austenite grains. The plates of acicular ferrite therefore radiate in many different directions from what are, in effect, point nucleation sites. The following features are common to acicular ferrite and bainite:

- They both display the incomplete reaction phenomenon *i.e.* reaction ceases before the equilibrium or paraequilibrium volume fraction of ferrite has formed. (Bhadeshia & Edmonds, 1979, 1980).
- Both the phases show surface displacements consistent with a macroscopic invariant plane strain (IPS) shape change. (Strangwood & Bhadeshia, 1987).
- Both phases can form ‘upper’ and ‘lower’ forms (Sugden & Bhadeshia, 1989) distinguishable by the presence or absence of carbide precipitation in the ferrite. Upper bainite and acicular ferrite have carbides precipitated only in the austenite between the ferrite plates. Lower bainite and lower acicular ferrite have carbides situated within the ferrite phase. There is a competition between the decarburisation of the supersaturated ferrite by partitioning of carbon into the austenite, and carbide precipitation from supersaturated ferrite. In upper bainite and upper acicular ferrite precipitation of carbides within the ferrite cannot occur rapidly enough to prevent complete decarburisation by diffusion into the surrounding austenite. (Takahashi & Bhadeshia, 1990)
- In reheated weld metals, forming acicular ferrite in the as-welded condition, bainite can be induced to form instead if the austenite grain size is reduced in order to increase the number density of grain boundary nucleation sites relative to those within the austenite grains (Yang & Bhadeshia, 1987). Alternatively, if grain boundary nucleation is inhibited by decorating the austenite grain surfaces with thin layers of allotriomorphic ferrite, then the acicular ferrite microstructure is recovered (Babu & Bhadeshia, 1990).

In view of the similarities between the acicular ferrite and bainite reactions it seems appropriate to apply the bainite kinetics theory to acicular ferrite, and to model development under conditions of continuous cooling.

6.3.2 Assumptions

The attempt to apply the improved theory of bainite transformation kinetics (Chapter 3) to acicular ferrite requires the following assumptions:

The thermodynamics of the two processes are considered to be the same (Yang & Bhadeshia 1987). This means that acicular ferrite has the same driving force and limiting volume fraction as bainite at any temperature below the bainite-start temperature.

The autocatalysis process and the value of the autocatalysis constant are assumed to be the same for acicular ferrite and bainite, despite the fact that acicular ferrite does not usually form sheaves. It is clear though, from the microstructures of some experimental welds that sheaf formation in acicular ferrite is indeed possible. It seems likely that impingement with the products of other nucleation events within the austenite grains is the factor that inhibits sheaf development for acicular ferrite.

6.3.3 Time-Temperature Profile of a Cooling Weld

The cooling behaviour of an arc weld can be well represented by the expression (Svensson, Gretoft & Bhadeshia, 1986)

$$\frac{dT}{dt} = \frac{\epsilon_1 (T - T_{\text{int}})^{1-\epsilon_2}}{Q\eta} \quad (6.1)$$

where the interpass temperature is represented by T_{int} . The electrical energy input Q and the arc transfer efficiency η are process-dependent variables. The terms ϵ_1 and ϵ_2 are material-dependent empirical constants. The expression can be integrated to give

$$t = Q\eta \left(\frac{(T_0 - T_{\text{int}})^{1-\epsilon_2}}{(1-\epsilon_2)} - \frac{(T - T_{\text{int}})^{1-\epsilon_2}}{(1-\epsilon_2)} \right) \quad (6.2)$$

where T_0 represents the initial temperature *i.e.* at $t = 0$, for convenience set at 900 °C. The submerged arc and manual metal arc welding processes are distinguished by the heat input and arc transfer efficiency terms. For the submerged arc welds investigated in the present work the values of ϵ_1 , ϵ_2 and η were (Svensson, 1988)

$$\epsilon_1 = 4359 \quad \epsilon_2 = 1.51 \quad \eta = 0.95$$

6.3.4 Application of the Bainite Kinetics Model to Continuous Cooling

As discussed in Chapter 3, the bainite kinetics expression can be expressed by the differential equation

$$\theta \frac{d\xi}{dt} = K_1(1-\xi)(1+\beta\theta\xi)I\{T, \xi\} \quad (6.3)$$

where the temperature dependence of the nucleation rate, as well as its dependence on the extent of reaction are represented in general form for brevity. The time dependence of temperature can be expressed by the cooling rate equation (eqn. 6.2), but quantities such as driving force and phase boundary compositions are calculated by iterative methods, and hence it is

impossible to express the time dependence of the bainite volume fraction as an explicit function of temperature.

For continuous cooling heat treatments it is therefore necessary to use a numerical summation to evaluate the volume fraction of bainitic ferrite formed as a weld cools. The calculation procedure is outlined below

- (1) If the maximum volume fraction of ferrite that can form at temperature T is θ , let the time t , taken to form an actual volume fraction v at temperature T be represented in a general form as

$$t = t \{v, T\} \quad (6.4)$$

The normalised volume fraction ξ formed after isothermal transformation at temperature T for time t is therefore

$$\xi = \xi \{t, T\} \quad (6.5)$$

where

$$v = \xi\theta \quad (6.6)$$

- (2) The time-temperature profile of the weld is separated into one degree steps, as shown schematically in Figure 6.1. The continuous cooling curve is therefore approximated as a series of short isothermal steps. At temperature T_i the duration of the isothermal hold is Δt_i , and the maximum allowable fraction of bainite or acicular ferrite is θ_i .
- (3) At step $i = 1$ the volume fraction of ferrite formed after the end of the first isothermal step Δt_1 is calculated. *i.e.*

$$v_1 = \theta_1 \xi \{ \Delta t_1, T_1 \} \quad (6.7)$$

- (4) At the second isothermal temperature, the effective time t_{e_2} necessary for formation of the fraction v_1 at this temperature is calculated *i.e.*

$$t_{e_2} = t \{v_1, T_2\} \quad (6.8)$$

- (5) The ferrite is then allowed to grow for the duration of the second isothermal hold Δt_2 .

$$v_2 = \theta_2 \xi \{t_{e_2} + \Delta t_2, T_2\} \quad (6.9)$$

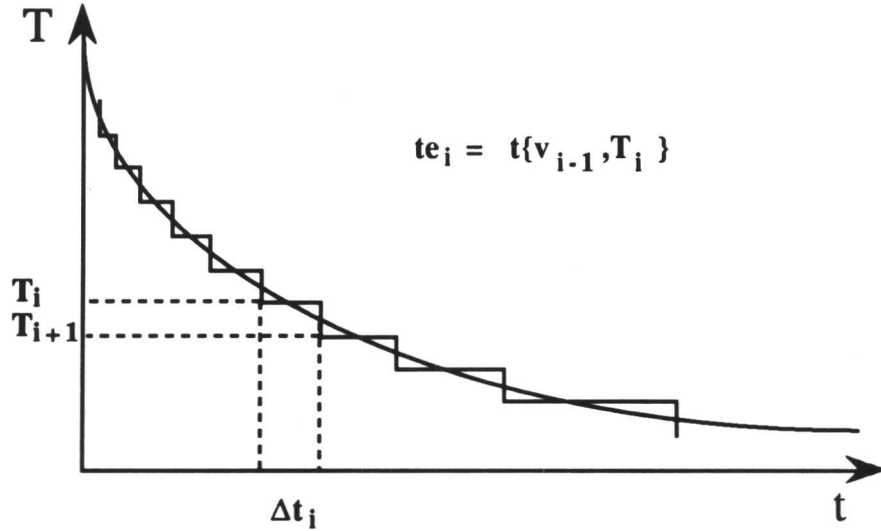


Figure 6.1 The approximation of a continuous time-temperature profile as a series of short isothermal steps. The isothermal step step length Δt_i is defined.

- (6) At subsequent temperatures T_i , the effective time t_{e_i} necessary to form the existing volume fraction is calculated. The calculated volume fraction for a general temperature is then v_i where

$$v_i = \theta_i \xi \{t_{e_i} + \Delta t_i, T_i\} \quad (6.10)$$

with

$$t_{e_i} = t \{v_{i-1}, T_i\} \quad (6.11)$$

Reaction-Start and Reaction-Finish Temperatures

Acicular ferrite, being similar to bainite, can only form when the appropriate thermodynamic criteria for nucleation and growth are satisfied. The criterion for growth is that (Bhadeshia, 1981a)

$$\Delta G^{\gamma \rightarrow \alpha} = -400 \text{ J mol}^{-1} \quad (6.12)$$

where $\Delta G^{\gamma \rightarrow \alpha}$ is the free energy change for transformation from austenite to ferrite of the same composition. The condition which must be satisfied for nucleation is that

$$\Delta G_m^0 < G_N \quad (6.13)$$

at the reaction temperature (Bhadeshia, 1982a). ΔG_m^0 represents the maximum free energy change for formation of a small amount of ferrite from austenite, and G_N is the universal function representing the value of ΔG_m at which nucleation by a displacive mechanism becomes possible.

Once the temperature of the cooling weld has fallen below M_S there is sufficient driving force to form martensite. Since martensite is favoured kinetically over bainite and acicular ferrite, it is assumed that the acicular ferrite formation stops once martensite formation has begun.

Attempts to account for the depression of the M_S temperature of the untransformed by carbon enrichment were not successful. Using the empirical expression for the estimation of the M_S (Bhadeshia, 1981b, 1981c) resulted in the prediction that the untransformed austenite would never transform to martensite since, as reaction to acicular ferrite proceeded the predicted M_S temperature decreased faster than the actual temperature.

6.3.5 Nucleation Site Density

Since it is known that the nucleation of bainite and acicular ferrite occurs on different sites, it is unlikely that the previously determined value of the nucleation site density dependent constant for bainite kinetics, K_1 , can be applicable to acicular ferrite. This constant was therefore varied in order to produce the best agreement between the predicted and experimental observed acicular ferrite fractions for the alloy series as a whole.

An attempt was made to weight the nucleation site density parameter in proportion to the calculated inclusions content (Kluken & Grong, 1989) of the weld (Figure 6.2). This involved multiplying the K_1 for each alloy, by a factor proportional to the inclusion content. The data in Figure 6.2 is presented according to the amount of oxygen present (ppm by weight) in each type of inclusion.

The following different methods for weighting were tried in order to investigate the potency of particular oxides

- (1) MnO content;
- (2) Al_2O_3 content;
- (3) combined Al_2O_3 and MnO content;
- (4) no weighting.

The computer program used for the calculation of the acicular ferrite volume fraction formed during continuous cooling is presented in Appendix 4.

6.4 Properties of High Strength Steel Welds

When phases are all present present in substantial fraction it is a convenient assumption to

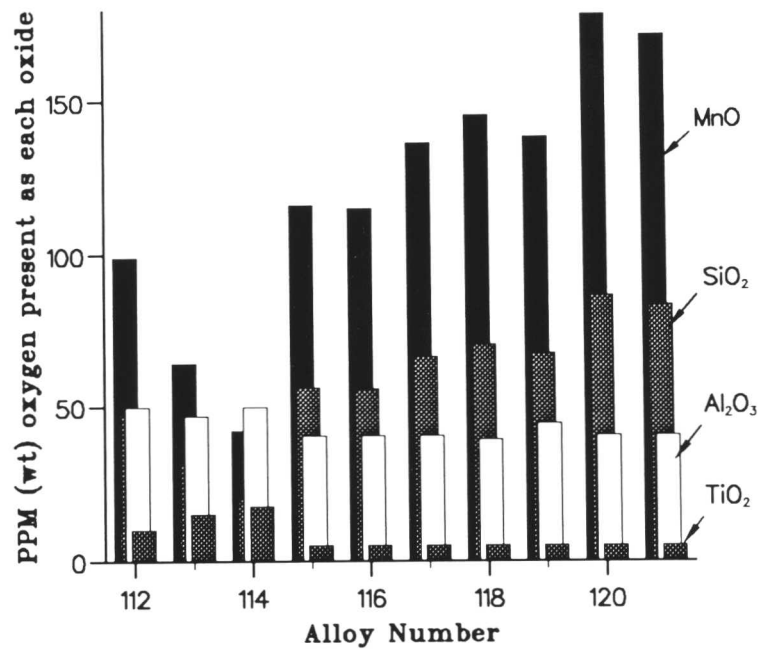


Figure 6.2 Calculated inclusion content of the alloys in the high strength weld metal series. The inclusion content is represented by the oxygen (ppm by weight) present as each oxide type.

suppose that the overall yield strength of a weld metal can be expressed as a ‘rule of mixtures’, in which each of the phases contributes according to its strength and volume fraction.

This assumption has been successfully applied by Sugden (1988) to estimate the strength of weld deposits containing allotriomorphic ferrite, Widmanstätten ferrite and acicular ferrite. Central to that work was the evaluation of the microstructural contribution to the strength of the phases *i.e.* different forms of ferrite have different strengths due to their different morphologies. This microstructural contribution to the strength of the deposit was determined for each of the phases. Acicular ferrite and the microphases were grouped together, and hence the microstructural strengthening term deduced for acicular ferrite actually applies to the combination of phases which this grouping can represent. Since, in many cases, the microphases were probably martensitic, it is possible that the microstructural contribution to the strength of acicular ferrite was overestimated. In any case, for present purposes, where microstructures consist of substantial amounts of both acicular ferrite and martensite, it is necessary to consider these phases separately.

Let σ_{α_a} , $\sigma_{\alpha'}$ and σ_y represent the yield stresses of the acicular ferrite, martensite and the resultant two-phase microstructure. Applying the ‘rule of mixtures’ approximation to the

strength of the weld deposit, the overall yield strength can be expressed as

$$\sigma_y = V_{\alpha_a} \sigma_{\alpha_a} + (1 - V_{\alpha_a}) \sigma_{\alpha'} \quad (6.14)$$

6.4.1 Modelling the Hardness of Martensite

The strength of martensite as function of alloy and carbon composition can be estimated using the empirical relationship for the Vickers hardness of martensite determined by Maynier, Jungmann & Dollet (1978) *i.e.*

$$HV = 127 + 949c_C + 27c_{Si} + 11c_{Mn} + 8c_{Ni} + 16c_{Cr} + 21 \log(V_R) \quad (6.15)$$

where c_i refers to the concentration of the i th element (wt %), and V_R represents the cooling rate experienced by the steel ($^{\circ}\text{Cs}^{-1}$). Unfortunately, this expression was determined for steels of rather higher carbon concentration than those under present investigation and so it was decided to establish our own empirical model for the hardness of martensite. Since carbon is known to affect the yield strength of steel in proportion to the square root of its concentration (Speich & Warlimont, 1968), and other elements in small concentrations are assumed to have a linear effect on strength, the form of the empirical expression for martensite hardness is

$$H_{\alpha'} = k_c c_c^{1/2} + \sum_i k_i c_i + k_0 \quad (6.16)$$

where k_i represents the coefficient of the strength contribution of i th element, of concentration c_i (wt%). The term k_0 is the contribution independent of alloy composition.

The relationship between the Vickers hardness and the 0.2% proof stress of a material can be approximated by (Cahoon *et al*, 1971)

$$\sigma_y = \left(\frac{H}{3} \right) (0.1)^{m-2} \quad (6.17)$$

where m is the Meyer's hardness coefficient, related to the strain hardening coefficient n by the expression (Tabor, 1951)

$$n = m - 2 \quad (6.18)$$

In the absence of strain hardening data for the weld deposits being considered here, it was decided to use the simplifying assumption

$$\sigma_y = \frac{H}{3} \quad (6.19)$$

despite the fact that Sugden (1987) has argued that this leads to an overestimation of yield strength.

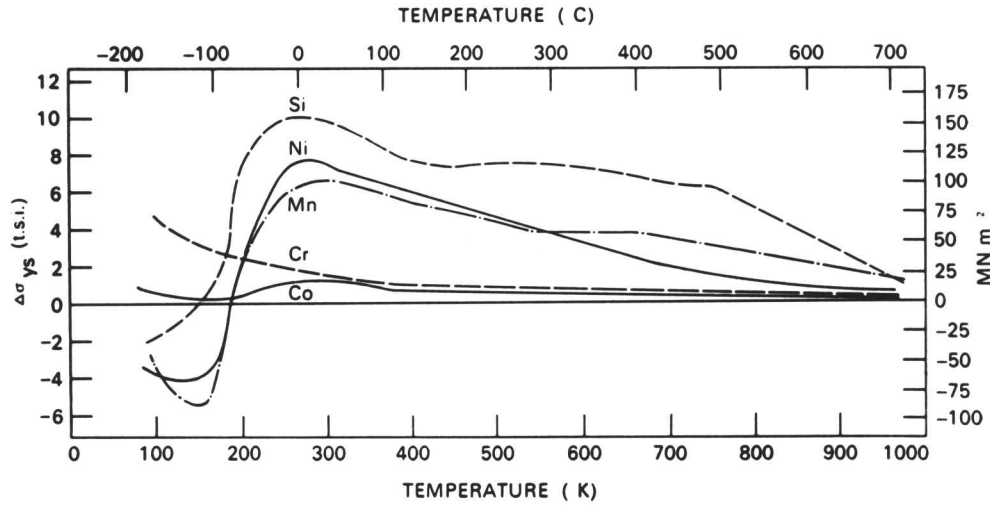


Figure 6.3 The solid solution strengthening effects of various alloying elements of iron (after Leslie, 1972)

The strength of the acicular ferrite in the microstructure was estimated by considering the effect of various substitutional and interstitial alloying elements. Since the solubility of carbon in ferrite is less than 10^{-3} (at%) at room temperature (Hansen, 1958) its solid solution strengthening effect on ferrite is considered negligible. Nitrogen present in the weld is considered to be present in solution. The solid solution strengthening effects of the elements were estimated using data from Leslie (1972). Figure 6.3 displays the solid solution strengthening effects of various substitutional alloying elements on iron (after Leslie 1972). In small concentrations the effect of each element can be combined linearly. The strength of acicular ferrite is then given by (Sugden 1988)

$$\sigma_{\alpha_a} = \sigma_{Fe} + \sum_i x_i \kappa_i + \Delta\sigma_{mic} \quad (6.20)$$

where x_i denotes the atomic fraction of element i . The κ_i value for each element is given in Table 6.1. The term $\Delta\sigma_{mic}$ represents the microstructural contribution to the yield strength of acicular ferrite, with σ_{Fe} representing the strength of pure annealed iron.

6.4.2 Experimental Technique

The macro-hardness (VHN) of the as-deposited weld metal was determined for the centre bead of the top layer of each weld. The tests were performed on specimens mounted, polished

Solid Solution Strengthening Coefficients (MPa/mole)	
κ_{Si}	5215
κ_{Mn}	3510
κ_{Ni}	3938
κ_{Cr}	94

Table 6.1 Coefficients of solid solution strengthening by substitutional solutes in ferritic iron (Leslie 1972).

and lightly etched in the same manner as used for metallography. The indentation load was 10 kg in all cases. Martensitic specimens were prepared by cutting samples (approximate dimensions 1cm \times 1cm \times 1cm) from the heart of each weld and quenching in iced water after and austenitisation treatment of 10 minutes at 1000°C. The specimens were sealed in quartz tubes under a partial pressure of pure argon during the austenitisation, with the tube being broken in the quenching bath immediately after removing from the furnace. The macro-hardness values of the martensitic specimens were also determined by taking the mean value from 10 measurements. Table 6.2 gives the composition and hardness values for the as-deposited and martensitic specimens of each alloy.

After determination of the hardness coefficients for martensite it is necessary to express the hardness of martensite in the two phase acicular ferrite and martensite mixture in the as-deposited weld metal. If the volume fraction of acicular ferrite is V_{α_a} then the carbon concentration of the austenite that transforms to martensite is

$$\frac{\bar{x} - x_{\alpha_a} V_{\alpha_a}}{(1 - V_{\alpha_a})} \quad (6.21)$$

making the hardness of the martensite

$$H_{\alpha'} = k_c \left(\frac{\bar{x} - x_{\alpha_a} V_{\alpha_a}}{(1 - V_{\alpha_a})} \right)^{1/2} + \sum_i c_i k_i + k_0 \quad (6.22)$$

The optimum value of the microstructural component of acicular ferrite strength was determined by re-arranging the equation for the total weld deposit hardness so that $\Delta\sigma_{mic}$ could be determined by regression. This was achieved by separating the equation for the overall alloy strength in the following way

$$\sigma_y - V_{\alpha_a} \left(\sigma_{Fe} + \sum_i x_i \kappa_i \right) - (1 - V_{\alpha_a}) \sigma_{\alpha'} = V_{\alpha_a} \Delta\sigma_{mic} \quad (6.23)$$

The left-hand side of the equation was plotted against V_{α_a} so that the gradient of a straight line fitted to the data, forced through the origin, gave the optimum value of $\Delta\sigma_{mic}$.

Alloy No.	C	Si	Mn	Ni	Mo	Cr	H_{tot}	$H_{\alpha'}$
90	0.071	0.30	1.22	2.02	0.39	0.49	277 ± 5	398 ± 10
112	0.062	0.26	1.30	2.18	0.38	0.44	264 ± 3	366 ± 5
113	0.059	0.47	1.48	2.00	0.37	0.63	276 ± 3	391 ± 7
114	0.079	0.53	1.64	2.32	0.42	0.69	328 ± 2	400 ± 5
115	0.059	0.48	2.02	2.2	0.41	0.65	297 ± 6	393 ± 6
116	0.053	0.46	1.08	2.2	0.41	0.65	263 ± 2	346 ± 5
117	0.054	0.46	1.53	3.01	0.41	0.66	296 ± 2	393 ± 4
118	0.052	0.44	1.51	1.52	0.41	0.66	268 ± 2	364 ± 5
119	0.067	0.47	1.53	2.13	0.57	0.64	297 ± 4	386 ± 5
120	0.052	0.44	1.58	2.18	0.24	0.64	257 ± 4	369 ± 4
121	0.052	0.42	1.51	2.23	0.41	0.90	292 ± 3	357 ± 6

Table 6.2 Compositions (wt%) and hardness values (VHN) of the as-deposited weld metal and martensitic specimens from the high strength weld metal alloy series.

The volume fraction measurements of acicular ferrite in the microstructures of the high strength weld deposits are listed in Chapter 5. These values, determined by point counting on high magnification SEM images, were used for the optimisation of σ_{mic} . The computer program for predicting the the hardness of the weld microstructures is presented in Appendix 5.

6.5 Microstructure Prediction Results

Figures 6.4, 6.5 and 6.6 show the best fit predictions of acicular ferrite volume fraction when the calculations were weighted according to the MnO content, the Al_2O_3 , the combined Al_2O_3 and MnO content respectively. The best results were, however obtained when no weighting was applied. The acicular ferrite volume fraction prediction for this condition is shown in Figure 6.7, and the agreement with the experimental volume fraction is shown in Figure 6.8 which plots the predicted versus the experimental values.

6.6 Hardness Prediction Results

The hardness coefficients for the martensite hardness expression were determined by a multiple regression algorithm. The best fit constants for this expression are displayed in Table 6.3 together with the standard errors. The optimum value of the microstructural contribution to the strength of acicular ferrite was determined by evaluating the gradient of the best-fit line shown in Figure 6.9. The determination of this value utilised the empirical expression for the

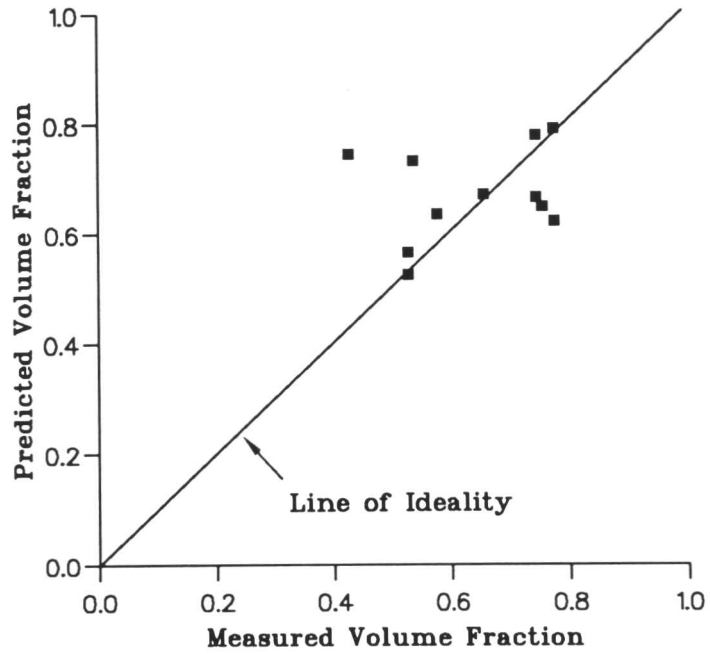


Figure 6.4 The best agreement obtained for predicted *vs.* experimentally measured volume fractions with calculations weighted according to the MnO content of the weld.

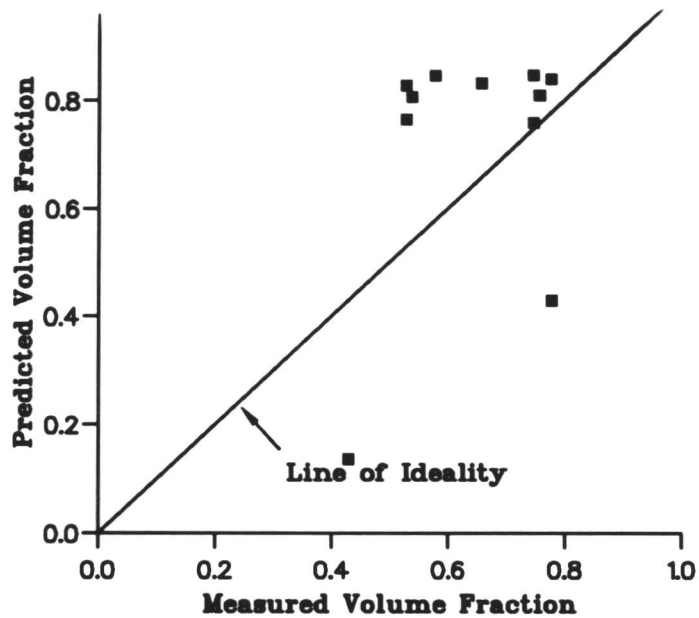


Figure 6.5 The best agreement obtained for predicted *vs.* experimentally measured volume fractions with calculations weighted according to the Al_2O_3 content of the weld.

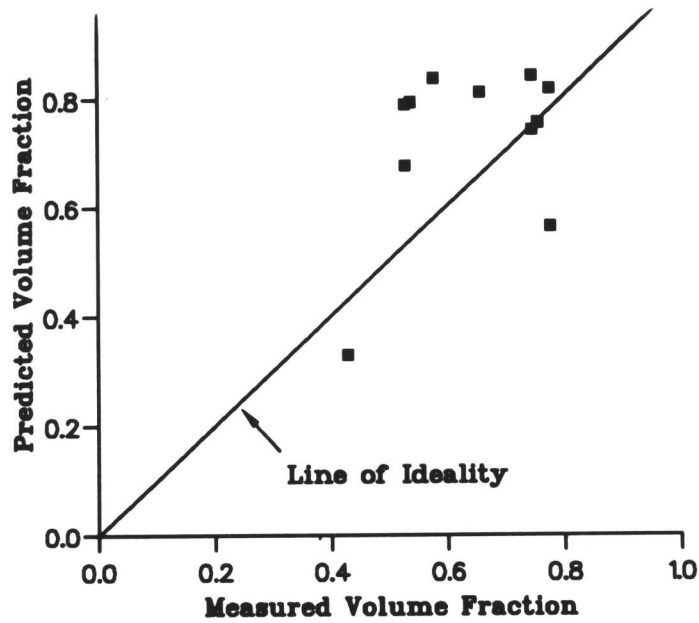


Figure 6.6 The best agreement obtained for predicted *vs.* experimentally measured volume fractions with calculations weighted according to the combined Al_2O_3 and MnO content of the weld.

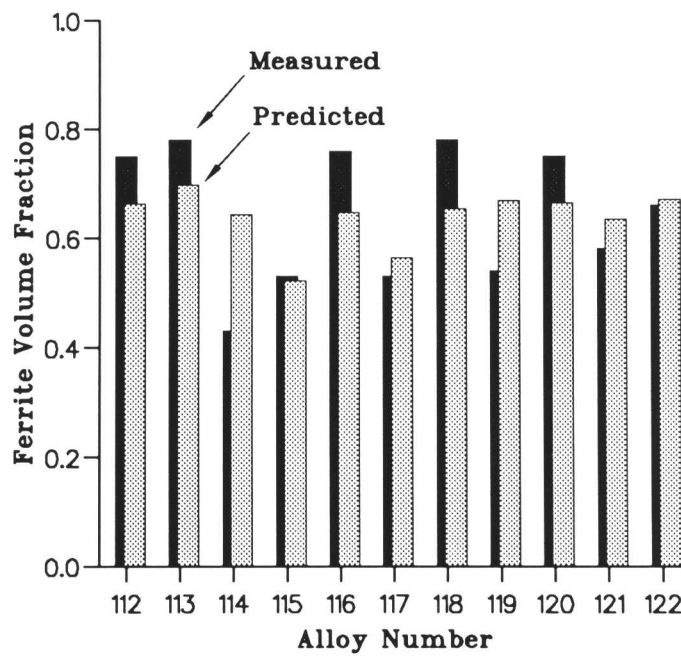


Figure 6.7 Histogram showing the predicted acicular ferrite volume fraction for the alloy series when no weighting was applied to the prediction calculation.

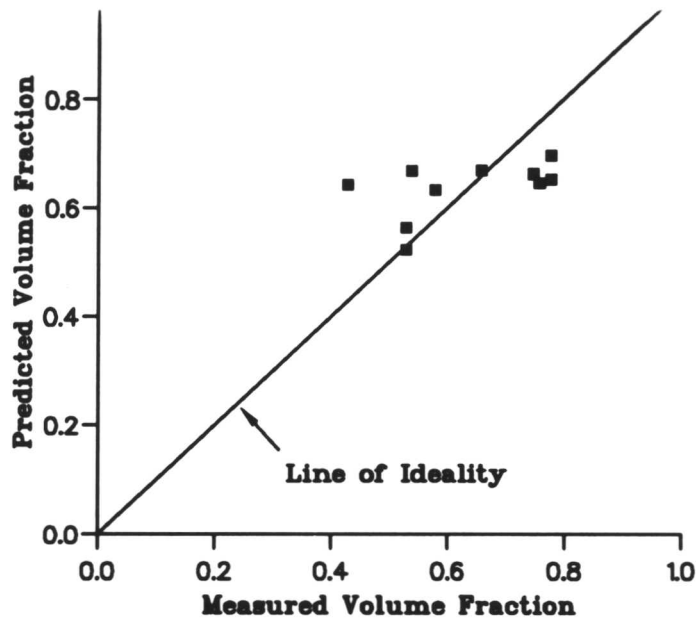


Figure 6.8 A plot of predicted volume fraction versus the experimentally measured volume fraction of acicular ferrite when no weighting was applied to the prediction calculation.

hardness of martensite. The result of this analysis was

$$\Delta\sigma_{\text{mic}} = 316 \pm 15 \text{ M Pa} \quad (6.24)$$

Using the optimised value of $\Delta\sigma_{\text{mic}}$ the hardness of the as-deposited weld microstructures were predicted using the experimentally determined values of the acicular ferrite volume fractions. The resulting agreement between the predicted and experimental hardnesses, shown in Figure 6.10 is good, with a correlation coefficient of 0.94.

6.7 Conclusions

6.7.1 Microstructure Prediction

As can be seen from the best fit prediction of acicular ferrite volume fraction, the trends in the microstructure resulting from the different substitutional solute content of the alloys are reflected correctly in the theoretical predictions. It is apparent however, that the microstructure of the actual weld deposits is more sensitive to the variations in alloy chemistry than the calculation suggest. While it is not clear why this is the case, it is stressed that the constants used in the theory were determined for high-silicon steels, varying only the nucleation site density constant. As will be explained in Chapter 9, it has not proved practical to establish

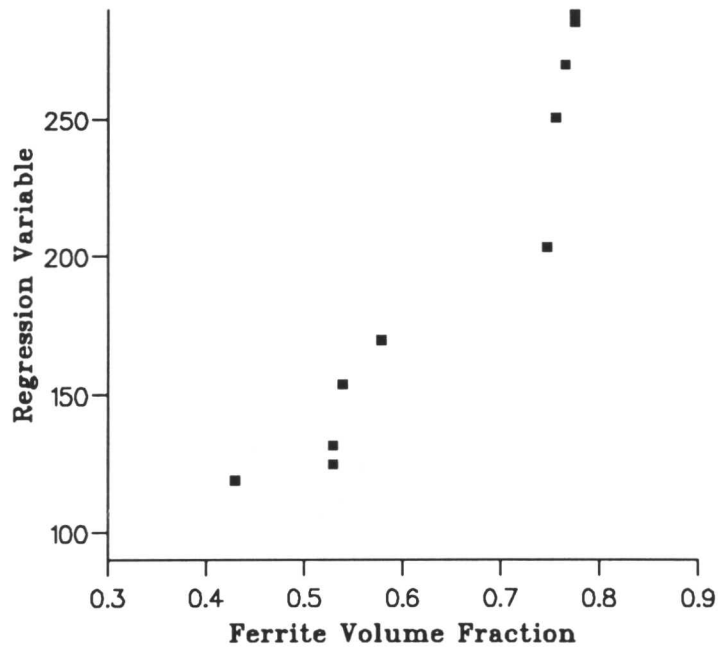


Figure 6.9 The determination of the microstructural component of the strength of acicular ferrite in the two-phase acicular ferrite and martensite structure of the high strength steel weld deposits. The regression variable is defined as $\sigma_y - V_{\alpha_a} (\sigma_{Fe} + \sum_i x_i \kappa_i) - (1 - V_{\alpha_a})$.

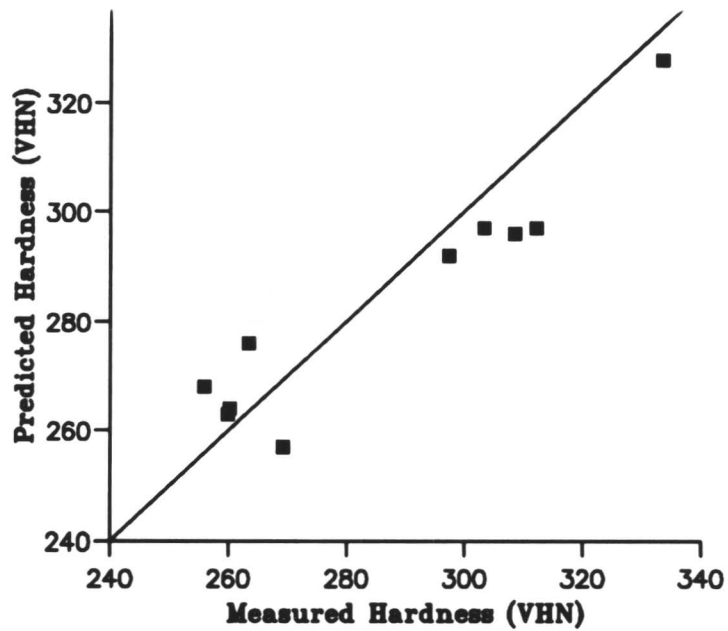


Figure 6.10 The degree of agreement between the predicted and the calculated hardness values of the high strength steels weld deposits.

Hardness coefficient	Regression Value (VHN)	Standard Error (VHN)
k_C	671	458
k_{Si}	-73	408*
k_{Mn}	35	27
k_{Ni}	13	16
k_{Mo}	-9	82*
k_{Cr}	60	418*
k_0	133	190

Table 6.3 Results of the regression analysis of the hardness of martensite as a function of alloy composition. Results where the standard error of a hardness coefficient is much greater than the determined value are denoted with *.

the appropriate constants for the acicular ferrite transformation by optimising agreement between the theory and experimental isothermal transformation data. The fact that *trends* in the microstructure are reflected correctly suggests that the application of constants determined for bainite is appropriate for acicular ferrite, but that the optimum values may not have been achieved.

6.7.2 Hardness Prediction

Experimental results and predictions from modelling indicate that increasing the volume fraction of martensite in the weld deposit will increase the overall hardness. Welds that have a high volume fraction of acicular ferrite are correctly predicted as being softer than those which have a high fraction of martensite, despite the fact that a high acicular ferrite fraction results in martensite with a higher carbon concentration. It may be the case however that small regions of high carbon martensite may be detrimental to overall toughness (the avoidance of high carbon martensite was a design aim of this type of weld deposit).

The agreement between predicted and experimental hardness values is good when using the experimentally determined volume fractions of acicular ferrite in the microstructure. It is also necessary to optimise the microstructural contribution to the strength of acicular ferrite in order to produce good results. It is interesting to note that the best fit value of $\Delta\sigma_{mic}$ is smaller than that the previously determined value (Sugden, 1988) where acicular ferrite was grouped together with the microphases in the structure. A possible explanation for this is that, in the original treatment, by grouping the acicular ferrite and microphases together, the strengthening effect of hard microphases (*e.g.* martensite) was attributed to acicular ferrite. The difference in the intrinsic strength of acicular ferrite determined by both these methods corresponds to 85

MPa *i.e.* around 28 HV only.

CHAPTER 7

The Effect of Austenite Grain Size on Bainite Transformation Kinetics

The purpose of this work is to investigate the validity of the well known assumption that the austenite grain size affects the transformation kinetics of bainite, and to rationalise the nature of any observed effects. As will be seen later there are some good reasons for a reinvestigation on theoretical grounds.

7.1 Experimental Procedure

A steel was chosen of a suitable composition, given in Table 7.1, that would enable the kinetics of bainitic transformation to be observed without the interference of carbide precipitation. The presence of silicon greatly inhibits the formation of cementite). Isothermal reaction kinetics were measured by monitoring the dilatation of a sample using a Thermo-mechmastor thermo-mechanical simulator. The kinetics are sufficiently slow in this steel for the time scale of the slight undershooting below the isothermal transformation temperature during quenching to be insignificant compared to the overall reaction time.

Alloy No.	C	Si	Mn	Ni	Mo	Cr	V
5763	0.16	2.00	1.46	0.02	–	–	–

Table 7.1 Composition of the steel used to investigate the effect of austenite grain size on the reaction kinetics of bainite. Composition values are in wt%.

Three different austenitisation treatments were applied in order to produce a large range of austenite grain sizes in the samples. After quenching to room temperature and tempering for 60 minutes at 600 °C the austenite grain structure of the specimens was examined using scanning electron microscopy and montage photographs containing numerous austenite grains were produced. The tempering process was applied with the object of enhancing the delineation of the prior austenite boundaries in the quenched microstructure (Yang, 1987). The grain size of the austenite was determined by deducing the mean linear intercept of a series of random lines with the outline of the austenite grains on these micrographs.

The isothermal heat treatment in the bainite temperature range was carried out on the three specimens after austenitisation at the different temperatures. The isothermal transformation temperature and cooling rate were identical for each sample, being set at 500°C and 40°Cs⁻¹ respectively. The specimens were mounted polished and etched in 2% nital before recording the microstructure using SEM.

It was also observed that the delineation of the austenite grains was more pronounced in the isothermally transformed specimens than in the specimens quenched to martensite and tempered. This enabled a measurement of the austenite grain size of the actual samples from which kinetic data were obtained. These results could then be compared with the values determined from the directly quenched martensitic specimens in order to confirm that the values agreed within the limits of experimental error.

The data of relative radius change, temperature and time were recorded in ASCII code and transferred from the thermomechanical simulator onto a SUN workstation for further analysis. Plots of relative radius change versus time were produced in order to compare the effect of the three different grain sizes on the transformation kinetics.

7.2 Results

Figures 7.1, 7.2 and 7.3 show micrographs of the samples austenitised for 3 minutes at 1300°C, 1200°C and 1000°C respectively. The grain size of the prior austenite is clearly markedly different in each specimen and as expected shows an increase as the austenitising temperature increases. Table 7.2 gives the mean linear intercept values determined for each sample in the quenched state. Figures 7.4, 7.5 and 7.6 show the microstructure of the specimens isothermally transformed at 500°C for 6 minutes. Figure 7.7 gives a comparison of the reaction profiles of these specimens, while Figure 7.8 confirms that the transformation kinetics at a lower temperature (480°C for 6 minutes) show similar results. Note that the time taken for transformation to approach its limiting value is greater than 100 s in all cases, whereas the duration of the undershooting below the isothermal transformation temperature is approximately 4 s.

Austenitisation Temp. $T_{\gamma}/^{\circ}\text{C}$	Mean Linear Intercept $\bar{L}/\mu\text{m}$
1300	234 \pm 30
1200	66 \pm 7
1000	36 \pm 4

Table 7.2 Mean linear intercept values for the prior austenite grain size of Alloy 5763, for three different austenitisation temperatures.

7.3 Discussion

As can be seen from Figures 7.7 and 7.8 the overall kinetics of transformation differ very little between samples of very different grain size. On the other hand, there is a marked

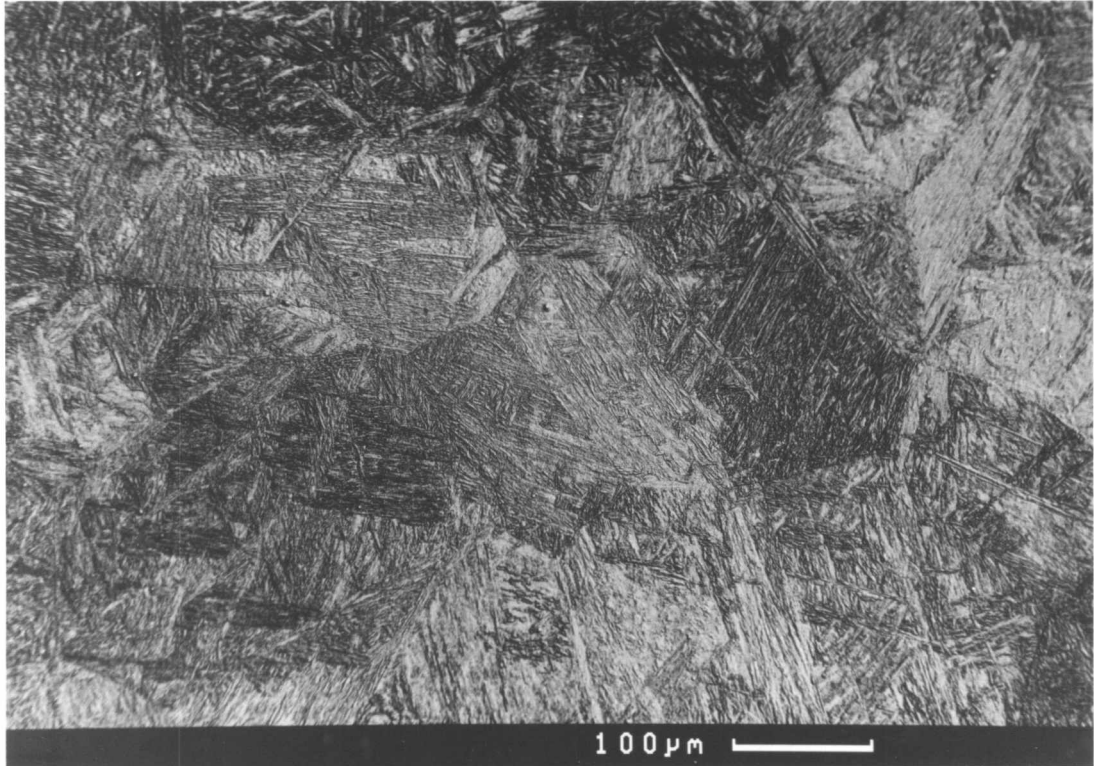


Figure 7.1 The microstructure of Alloy 5763 after austenitisation at 1300°C for 3 minutes followed by cooling at $40^{\circ}\text{C s}^{-1}$ to room temperature. The microstructure is martensitic.

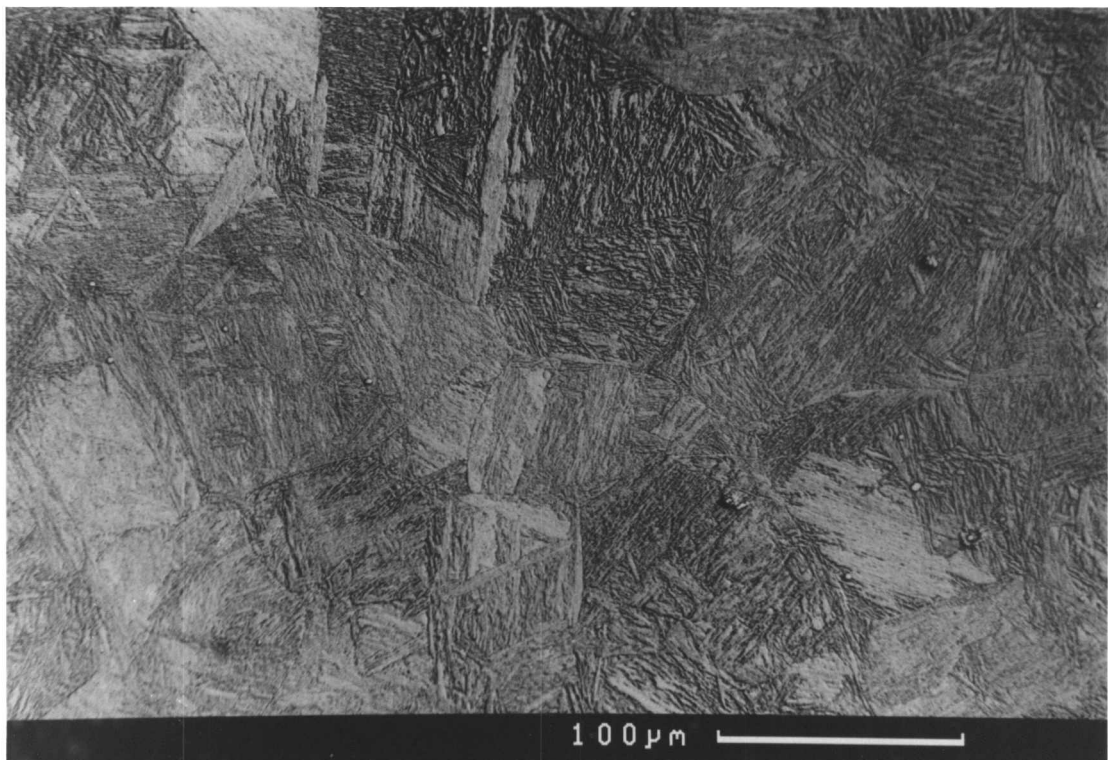


Figure 7.2 The microstructure of Alloy 5763 after austenitisation at 1200°C for 3 minutes followed by cooling at $40^{\circ}\text{C s}^{-1}$ to room temperature. The microstructure is essentially similar to that shown in Figure 7.1

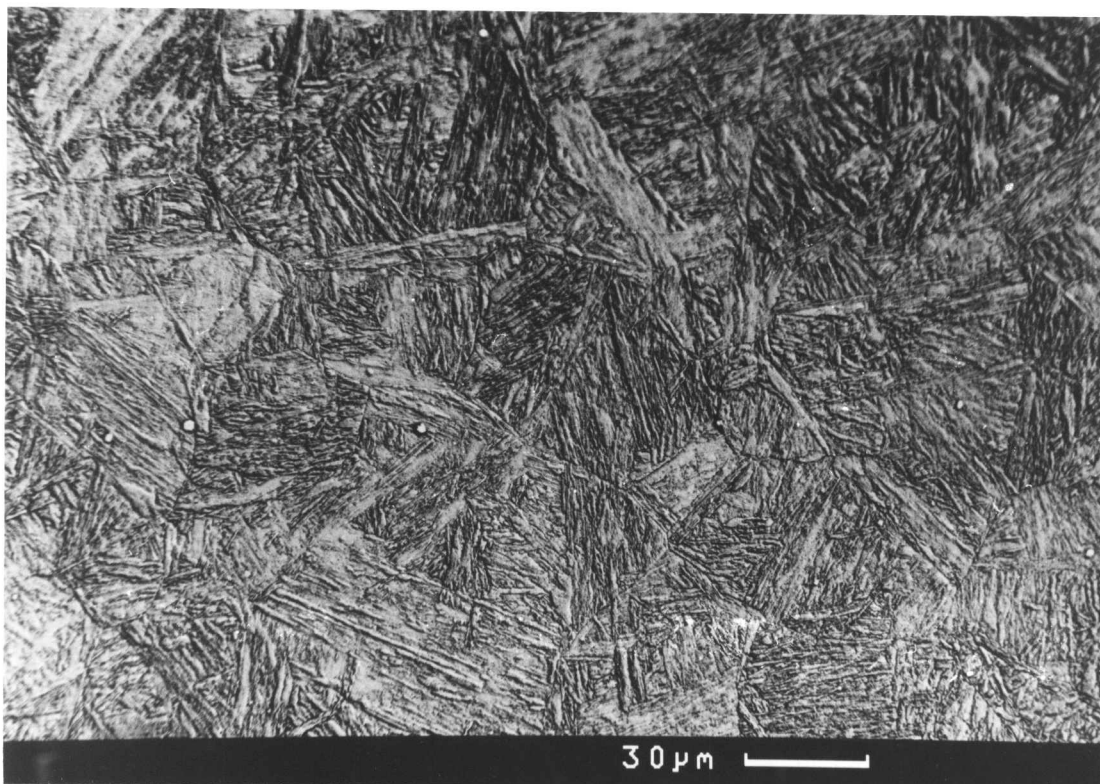


Figure 7.3 The microstructure of Alloy 5763 after austenitisation at 1000°C for 3 minutes followed by cooling at $40^{\circ}\text{C s}^{-1}$ to room temperature. The microstructure has a fine austenite grain structure, clearly visible at this magnification



Figure 7.4 The microstructure of Alloy 5763 after austenitisation at 1300°C for 3 minutes followed isothermal transformation at 500°C to room temperature.

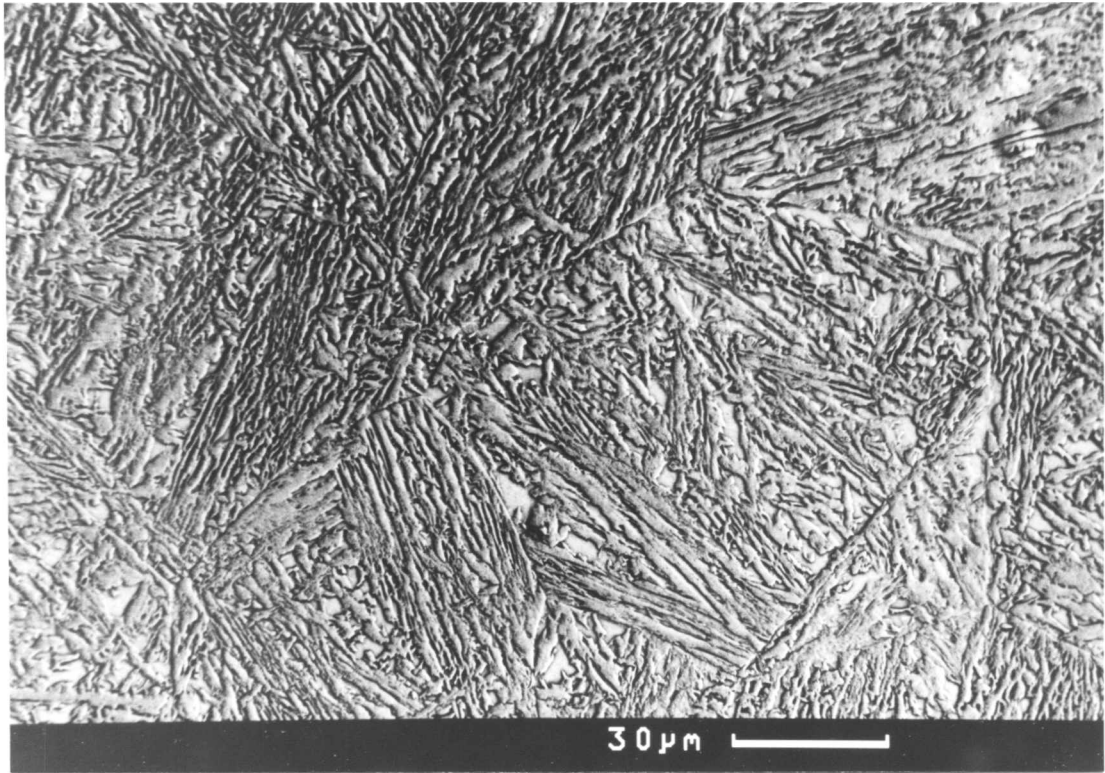


Figure 7.5 The microstructure of Alloy 5763 after austenitisation at 1200°C for 3 minutes followed isothermal transformation at 500°C to room temperature.

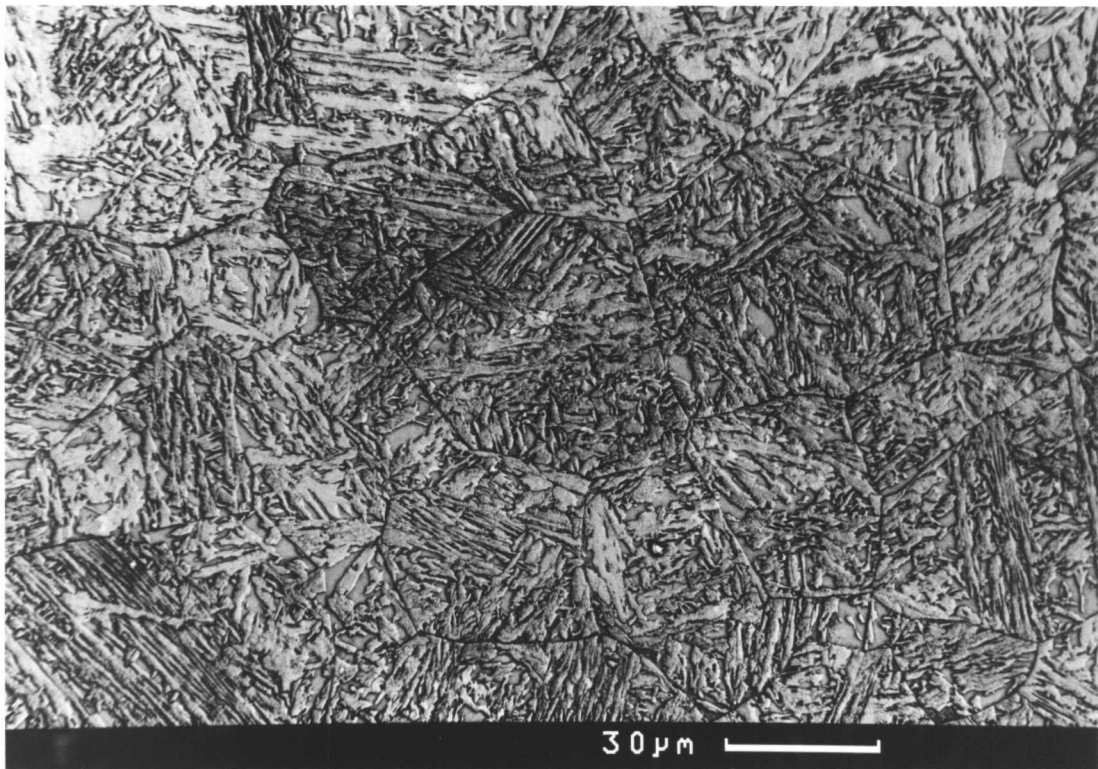


Figure 7.6 The microstructure of Alloy 5763 after austenitisation at 1000°C for 3 minutes followed isothermal transformation at 500°C to room temperature. The bainitic microstructure has a clearly defined prior austenite grain size.

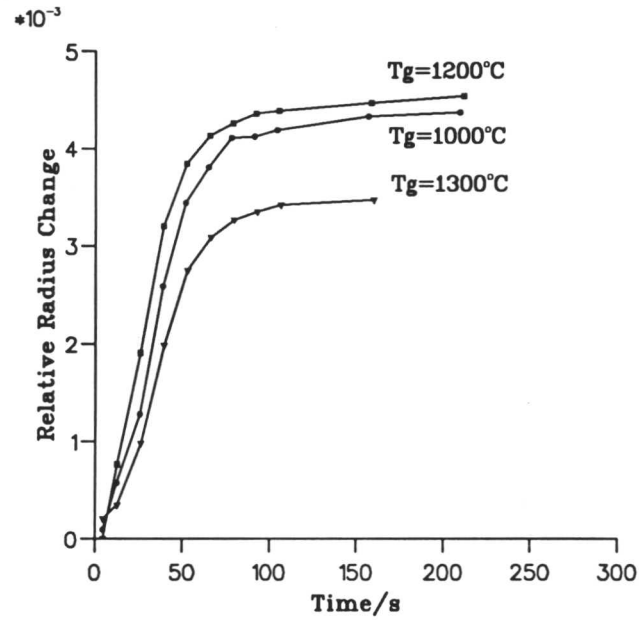


Figure 7.7 Comparison of the reaction profiles obtained by thermomechanical simulator transformation of Alloy 5763 of three different γ grain sizes at 500°C. The reaction rate of the three specimens is shown to be very similar.

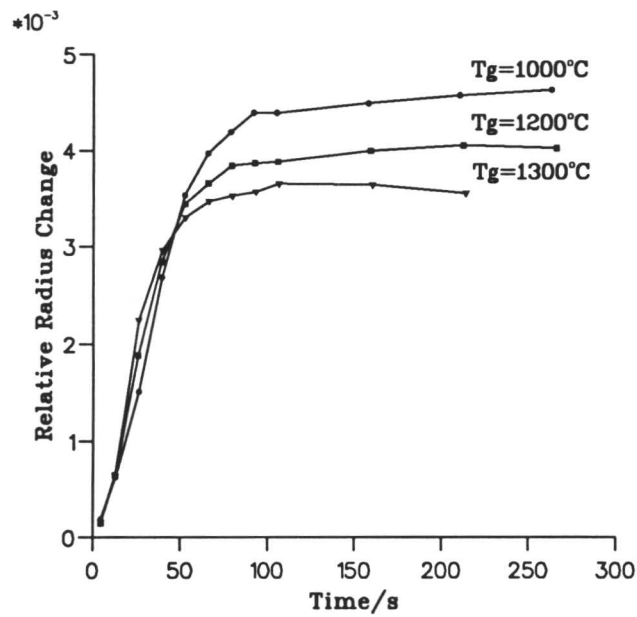


Figure 7.8 Comparison of the reaction profiles obtained by thermomechanical simulator transformation of Alloy 5763 of three different γ grain sizes at 480°C. The similarity in transformation kinetics for specimens of different grain sizes is again remarkable.

difference in the microstructure of the transformed specimens. The steels with the largest grain size, whose microstructure is shown in Figure 7.4, has extremely large sheaves, crossing the entire width of some grains. This is in contrast to the small grained specimen (Fig 7.6) in which the sheaves, while occasionally filling the grains, have a different appearance altogether, being shorter, and appearing to result from a greater number of separate grain boundary nucleation events. This results in more impingements between sheaves. It is interesting to note that the limiting relative radius change achieved depends on the austenite grain size of the specimen. While, for the two reaction temperatures investigated, the trend is not the same it is possible to speculate that this may be an effect due to the amount of blocky austenite trapped between large sheaves being greater in the case of the very large grained specimen. It is emphasised that the specimen with the largest grain size shows the smallest relative radius change at both transformation temperatures.

Simple considerations of grain boundary nucleated transformation products would suggest that the reaction rate of such phases would increase as the grain boundary area per unit increased. For martensite formation, however, it has been found that a decrease in the grain size depresses the martensite start temperature, when measured by comparatively insensitive techniques such as electrical resistance or dilatation (Cohen, 1991), despite the fact that the available sites for nucleation are expected to be more numerous for smaller grain sizes. More sensitive techniques such as acoustic emission actually reveal the opposite trend. These results can be rationalised by considering the volume of the product phase formed per grain boundary nucleation event. In martensite, where the plates tend to grow to the size of the parent grain, and autocatalysis effects can cause a burst of further transformation, the volume of ferrite formed per nucleation event is larger in the case of a larger grained specimen.

For the case of bainite, a rationalisation of the observed effect of grain size can be presented generally as follows. Consider the development of each individual sheaf. If the sheaf nucleates at time τ the normalised volume fraction of bainitic ferrite at that time is ξ , the normalisation is, as before, with respect to the appropriate limiting volume fraction. It is postulated that the possible number of sub-units which can grow within a sheaf is limited by a maximum value, denoted N_m . If N represents the number of sub-units in the sheaf at a given instant in time, then the rate of plate nucleation within a sheaf nucleated at time τ is

$$\frac{dN}{dt} = (1 - N/N_m) I \{\xi, N\}$$

where $I \{\xi, N\}$ where $I_{\xi, N}$ represents the nucleation rate of sub-units within the sheaf, which is a function of N and also of ξ , (since the extent of total transformation to ferrite will affect the austenite composition in which nucleation is occurring). The term $(1 - N/N_m)$ accounts

for the extended volume effects on sub-unit nucleation, bringing nucleation to a stop when the sheaf has reached its limiting size.

The effect of autocatalysis can be expressed as follows

$$I \{ \xi, N \} = (1 + \lambda_1 N) I_0 \{ \xi, N \}$$

where λ_1 is the autocatalysis constant for nucleation within a sheaf, and $I_0 \{ \xi, N \}$ represents the nucleation rate independent of autocatalysis, which, due to effects like carbon enrichment of the austenite surrounding the sheaf, is also function of N . Therefore

$$\frac{dN}{dt} = I_0 \{ \xi, N \} (1 + \lambda_1 N) (1 - N/N_m)$$

The volume of a sheaf at a given time will be the multiple of the number of sub-units with the sub-unit volume u .

If the nucleation rate per unit volume at grain boundaries, (effectively, the nucleation rate of sheaves), denoted $I_{Sh} \{ \xi \}$, is linearly dependent on the austenite grain surface per unit volume S_V it will be inversely dependent on the grain diameter represented by the mean linear intercept \bar{L} *i.e.*

$$I_{Sh} = I'_{Sh} / \bar{L}$$

where I'_{Sh} represents the contribution to I_{Sh} which is independent of the grain diameter. The nucleation rate is a function of the normalised volume fraction ξ of the bainite reaction.

Considering the overall transformation kinetics, the increment in volume fraction caused by the growth of a sheaf nucleated between τ and $\tau + d\tau$ is

$$\theta d\xi = \left((1 - \xi) u I_{Sh} \{ \xi \} \int_{\tau}^t \left(\frac{dN}{dt'} \right) dt' \right) d\tau$$

therefore

$$\frac{d\xi}{d\tau} = \frac{I'_{Sh} \{ \xi \} u (1 - \xi)}{\theta \bar{L}} \int_{\tau}^t \left(\frac{dN}{dt'} \right) dt'$$

where θ is the maximum allowable extent of transformation, and as mentioned above

$$\frac{dN}{dt} = I_0 \{ \xi, N \} (1 + \lambda_1 N) (1 - N/N_m)$$

It is assumed that I_0 itself is a function of ξ since the degree of carbon enrichment of the untransformed austenite is likely to be different for sheaves nucleating at the beginning and at later stages of transformation.

Examination of these expressions indicates that the transformation kinetics can be affected in two ways by increasing the grain size of the transforming austenite. If the effect of increasing the maximum allowable size of a sheaf counteracts the diminished nucleation rate at the grain

boundaries then the increase in transformation kinetics with increasing grain size can be rationalised. Also to be considered however is the exact interplay between autocatalytic and grain boundary nucleation. If autocatalytic nucleation is much faster than the grain boundary process and dominates over it then the effect on kinetics of increasing the sheaf size is expected to dominate *i.e.* kinetics will increase since a much larger amount of ferrite can form very rapidly. If both nucleation rates are comparable, then the decrease in the grain size will enhance the grain boundary nucleation, with further nucleation of sheaves possible within the time taken for a sheaf to reach its limiting size. Under these conditions it would be expected that a smaller grain size would increase the transformation kinetics. A qualitative understanding of the observed phenomena is therefore possible but at present it is not possible to account for these effects in a quantitative manner.

CHAPTER 8

The Required Driving Force for Nucleation of Displacive Transformations

8.1 Introduction

The current technological importance of bainite and acicular ferrite is immense. Accurate modelling of the kinetics of these transformations is highly desirable for the purpose of alloy design. Understanding the thermodynamics of transformation is obviously vital in the modelling process.

Recent work has indicated that there are many important similarities between bainite and acicular ferrite. Advances in the understanding of the bainite transformation may therefore be applied to the acicular ferrite reaction. It is known that both acicular ferrite and bainite exhibit ‘incomplete reaction’ *i.e.* under isothermal conditions, the reaction is observed to cease well before the equilibrium, or paraequilibrium ferrite volume fraction has formed (Bhadeshia & Edmonds, 1979, 1980; Yang & Bhadeshia, 1987; Strangwood & Bhadeshia, 1987). Both phases also produce surface relief consistent with a macroscopic invariant plane strain (IPS) shape deformation (Strangwood & Bhadeshia, 1987), as well as occurring in both the ‘upper’ and ‘lower’ forms (Sugden & Bhadeshia, 1989). The essential difference between the phases lies in the fact that bainite nucleates on prior austenite grain boundaries, whereas acicular ferrite nucleates on non-metallic inclusions present in the steel. The inclusions are either trapped as oxides during the welding process, or are the result of deliberate additions made via the flux.

It has not, however, been established that the thermodynamic criteria for nucleation are identical for both phases, and since the location of nucleation events is different in the two cases, it is of great interest to investigate the effect that this may have on the thermodynamics of nucleation.

8.2 The Minimum Driving Force for Bainite Nucleation

It has been found that in general, the minimum required driving force for nucleation of bainite is a linear function of temperature (Bhadeshia 1981). It was also shown that the required driving force for the nucleation of Widmanstätten ferrite also follows the same relationship, indicating that the process of nucleation for these two phases is identical. The results suggest that during the nucleation of bainite carbon partitioning occurs, whereas during the growth process the transformation is diffusionless, with the carbon supersaturation being relieved after the formation of each bainitic sub-unit. The incomplete reaction phenomenon characteristic of bainite is a direct result of this transformation mechanism, since the plate formation stops

when the untransformed austenite becomes sufficiently carbon-enriched to be unable to support further diffusionless transformation. Since acicular ferrite shows the same incomplete reaction phenomenon (Yang & Bhadeshia, 1987; Strangwood & Bhadeshia, 1987), it is assumed that its growth process is similar to that of bainite.

The fact that a linear relationship is observed between the driving force and the maximum temperature at which bainite formation can occur may be rationalised if it is considered that a minimum nucleation rate N is required for transformation to be observed. The relationship between N and the activation energy G^* can be expressed as follows

$$N = \nu \exp \left\{ -\frac{G^*}{RT} \right\}$$

where ν is the attempt frequency. Transformation will begin once the undercooling below Ae_3 is sufficient to achieve the necessary driving force.

By rearrangement it is possible to show that the activation energy G^* is a linear function of temperature.

$$G^* = RT \ln \left\{ \frac{\nu}{N} \right\}$$

When the available driving force is plotted against the highest temperature at which displacive transformations are observed a linear relationship is obtained (Bhadeshia 1981). This observation suggests that the activation energy for bainite nucleation is also a linear function of driving force, making it consistent with the theory of isothermal martensite nucleation kinetics (Olson & Cohen, 1976).

8.2.1 *The Nucleation of Acicular Ferrite*

There has been considerable speculation concerning the nucleation mechanism of acicular ferrite on inclusions. It has been proposed the elastic stress fields around the non-metallic inclusions arising from differential thermal contraction during cooling could assist nucleation, or that plastic strains resulting from the thermal contraction around inclusions provide a source of nucleating defects, enabling displacive transformation to ferrite (Bhadeshia & Christian, 1990). It has already been proposed that grain boundaries provide defects for nucleation of bainite, but these defects obviously do not occur as a result of thermal contraction, since there is no difference in expansion coefficients between neighbouring grains. Other proposals for the nucleation mechanism for acicular ferrite include the suggestion that certain oxide structures can cause local decreases in carbon level, causing an increase in local driving force, thereby activating existing structural defects in the austenite matrix (Strangwood 1986). Another popular idea is that the 'lattice matching' between the inclusion and the ferrite determines why some inclusion species appear more potent as nucleating sites than others. Mills, Thewlis & Whiteman (1987) suggest that there may be a reproducible orientation relationship between

the ferrite and the inclusion, though other experiments refute this suggestion (Dowling, Corbett & Kerr, 1986).

In all cases it is clear that the possibility exists for a significant difference in nucleation thermodynamics between acicular ferrite and bainite.

8.3 Experimental Procedure

Dilatometry was carried out using two pieces of apparatus, a THETA industries dilatometer (of the push rod variety) and a THERMECMASTOR thermo-mechanical simulator (TMS). A series of welds with systematic variations in deposit chemistry was provided by ESAB AB (Sweden). The compositions of these welds are given in Chapter 4, Table 4.1. Samples for dilatometry were prepared by cutting sections parallel to the weld centerline from the heart of each weld, well away from the areas of possible base plate dilution. These sections were hot swaged down to rods of the appropriate diameter. After homogenisation for three days at 1200 °C, in sealed quartz tubes under a partial pressure of argon, the outer layer of the rods was removed to eliminate any oxidised or decarburised surface. All specimens were nickel plated in order to minimise the possibility of decarburisation during austenitisation and surface nucleation during transformation. The specimen diameters for the THERMECMASTOR and the dilatometer were 6 mm and 3 mm respectively, with the respective lengths being 12 mm and 15 mm.

A characteristic of welding alloys with compositions similar to those in the experimental alloy series is that the kinetics of transformation to allotriomorphic ferrite are rather slow, resulting in as-deposited microstructures containing little or no allotriomorphic ferrite at prior austenite grain boundaries. Continuous cooling experiments at appropriate cooling rates can therefore be performed whilst completely avoiding all reconstructive transformations. The difference in the substitutional solute content of the weld metals does however require that faster cooling rates are applied to the lower alloy content variants, in order to avoid allotriomorphic ferrite formation.

Isothermal transformation experiments on these alloys indicate that the acicular ferrite reaction ceases in a matter of seconds. Combined with this is the fact that most predicted B_s temperatures for these alloys is nucleation limited *i.e.* the thermodynamic criterion for nucleation of bainite is satisfied at lower temperatures than the growth criterion. This criterion implies the presence of a flat-top lower C-curve in the TTT diagram for all steels in the alloy series. This is convenient for the present purposes since if the transformation-start temperature remains constant for two different cooling rates, then that temperature can be taken to represent the flat top. The cooling rates applied to the alloys over the temperature range of the lower C-curve were determined by the need to avoid reconstructive transformations whilst ensuring

that the cooling was sufficiently slow that transformation was detected at the highest possible temperature.

8.3.1 Austenite Grain Size

For acicular ferrite formation large austenite grains are required in order to reduce interference from the effects of grain boundary nucleated bainite. The dilatometer specimens were heat treated for 10 minutes at 1375°C to induce the growth of sufficiently large austenite grains. Such a treatment produces an extremely large grain size. Later work carried out on the TMS used an austenitisation treatment of 3 minutes at 1350°C, the shorter treatment being chosen to reduce the risk of decarburisation. Consistency between the microstructures produced by both treatments indicate that the grain size produced by the austenitisation treatment in the TMS was sufficient for intragranular effects to dominate those originating at the austenite grain surfaces.

Bainite formation requires the nucleation at grain boundaries to dominate over any intragranular nucleation. A small austenite grain size was therefore desirable for bainite formation. This was achieved by austenitising for 5 minutes at 1000 °C. Determination of the onset temperature was carried out on the TMS, since its superior vacuum system enabled the problem of decarburisation of the specimen surface to be eliminated. The earlier microstructural work carried out on the dilatometer showed that the transformation onset temperature increased as austenitisation times at high temperatures were increased. Observation of the microstructure of these specimens close to the surface confirmed that significant decarburisation had occurred. Microstructural observations on these specimens were therefore confined to central areas, well away from the surface.

Further precautions were taken to ensure that the problem of surface decarburisation was eliminated. The specimen chamber was purged with argon gas three times before pumping down to $\approx 2 \times 10^{-2}$ Pa prior to the austenitisation treatment. In the case of the high austenitisation temperature experiments with slower cooling rates, transformation was interrupted at an intermediate temperature in order to investigate the microstructure of the products formed at temperatures immediately below the onset temperature. By this method the location of transformation initiation could be determined more easily.

8.3.2 Determination of the Onset Temperature

Figure 8.1 shows schematically the procedure by which the transformation onset temperature was determined. The approximately linear contraction at higher temperatures indicates that no transformation is occurring. A straight line is fitted to this portion of the curve. Significant deviation from this straight line indicates the onset temperature of transformation

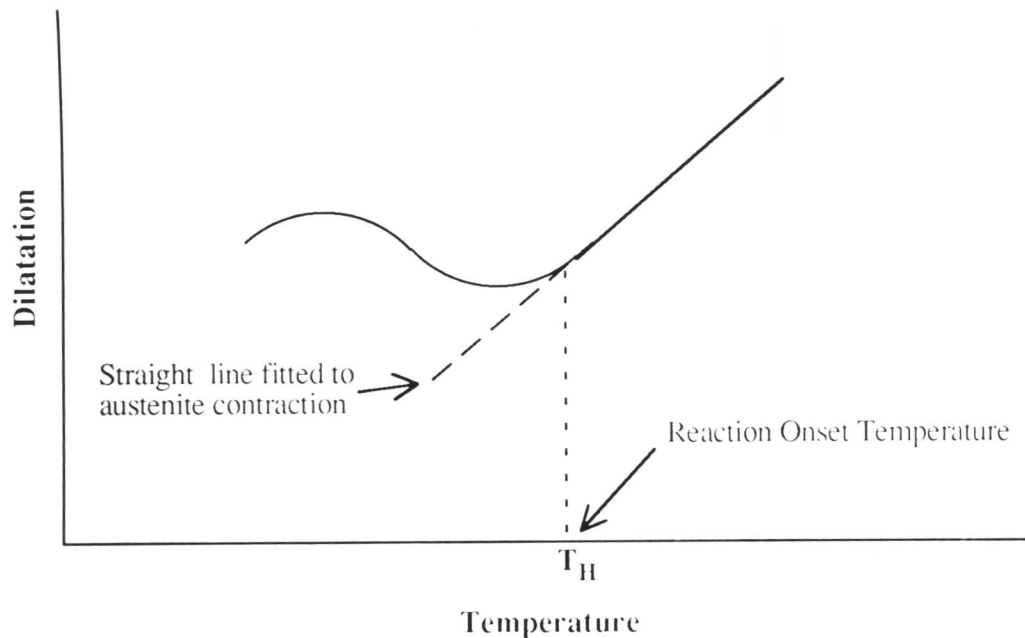


Figure 8.1 Schematic illustration of the method of determining the transformation onset temperature from dilatometric data.

T_H .

8.3.3 Determination of the Required Driving Force for Nucleation

Using the theory outlined in Chapter 2 the values of ΔG_m , the maximum free energy change on nucleation were determined for the alloy compositions at the experimentally determined T_H values. These results were used to construct plots of ΔG_m versus T_H for nucleation in the large and small austenite-grained specimens, representing acicular ferrite and bainite respectively.

8.4 Results

Table 8.1 shows the transformation onset temperatures T_H observed after the different austenitisation treatments. The temperatures shown are the highest determined values from experiments with cooling rates between 5°Cs^{-1} and 0.5°Cs^{-1} for the lightly alloyed members of the series and between 0.5°Cs^{-1} and 0.05°Cs^{-1} for the more highly alloyed variants. Comparison between onset temperatures determined from more than one cooling rate was used to establish that the highest temperature of the lower C-curve was reliably established, and that slower cooling would not result in a higher onset temperature. Included in Table 8.1 are the values of ΔG_m corresponding to the transformation onset temperatures. A plot of ΔG_m versus T_H is displayed in Figure 8.2 in which both high-temperature and low-temperature austenitisation

onset temperatures are shown.

Best fit lines were determined for the relationship between T_H and the driving force ΔG_m available at these temperatures. The regression equation for transformation to acicular ferrite is

$$\Delta G_m \{T_H\} = 3.112 T_H - 2163 \text{ J mol}^{-1}$$

(for T_H specified in °C). The correlation coefficient for the best fit straight line was 0.967. The standard error for the regression coefficient and constant were 0.28 and 149 respectively.

For transformation to bainite, in the small-grained specimens, the regression equation was

$$\Delta G_m \{T_H\} = 3.127 T_H - 2153 \text{ J mol}^{-1}$$

which has a correlation coefficient of 0.97. In this case the standard error in the regression coefficient and constant were 0.25 and 133 respectively.

Selected microstructures of the the transformed specimens are shown in Figures 8.4 to 8.10. The displayed micrographs reflect the different microstructures formed by the cooling processes, as a function of alloy content. For this purpose the high and low manganese variants of the alloy series, alloys 115 and 116 respectively, were singled out for examination. Table 8.2 gives the exact heat treatments experienced by the steels in each micrograph.

Alloy No.	$T_\gamma = 1000^\circ\text{C}$		$T_\gamma = 1350^\circ\text{C}$	
	T_H	ΔG_m	T_H	ΔG_m
112	563°C	-407	551°C	-472
113	550°C	-434	558°C	-390
114	510°C	-562	520°C	-507
115	480°C	-656	484°C	-634
116	570°C	-390	582°C	-325
117	511°C	-519	508°C	-524
118	568°C	-373	564°C	-395
119	520°C	-551	521°C	-545
120	552°C	-384	526°C	-526
121	514°C	-567	523°C	-522
122	540°C	-462	556°C	-375

Table 8.1 Transformation onset temperatures for the small-grained and large-grained specimens (*i.e.* the onset temperatures for transformation to bainite and acicular ferrite respectively). Also shown is the driving force at onset.

Figure No	Alloy	T_γ	Austenitisation Time	Cooling Rate	Apparatus
8.3	116	1375°C	10 min	5°Cs ⁻¹	Dilatometer
8.4	116	1350°C	3 min	0.5°Cs ⁻¹	TMS
8.5	115	1375°C	10 min	5°Cs ⁻¹	Dilatometer
8.6	115	1350°C	3 min	0.05°Cs ⁻¹	TMS
8.7	116	1000°C	5 min	5°Cs ⁻¹	Dilatometer
8.8	116	1000°C	5 min	0.5°Cs ⁻¹	Dilatometer
8.9	115	1000°C	5 min	5°Cs ⁻¹	Dilatometer
8.10	115	1000°C	5 min	0.05°Cs ⁻¹	Dilatometer

Table 8.2 Apparatus and austenite details of continuously cooled transformations.

8.5 Discussion

8.5.1 Onset Temperatures

The onset temperatures for reaction to acicular ferrite and bainite in the small grained specimens show the expected linear relationship between ΔG_m and T_H . It is interesting to note that the driving force versus onset temperature data for both acicular ferrite and bainite formation regress onto almost identical best-fit straight lines, despite the fact that the individual alloys show small changes in T_H following the different austenitisation treatments. There is no systematic trend in these small variations. Also noteworthy is the close agreement between the determined regression equations and that obtained by Ali & Bhadeshia (1990) from the data of Steven & Haynes *i.e.*

$$G_N = 3.636 T_H - 2540 \text{ J mol}^{-1}$$

The discrepancy between the two expressions, indicated in Figure 8.2, suggest that it is somewhat easier to nucleate displacive transformations in the welding alloys than in the steels studied by Steven & Haynes. A possible reason for this is that the low carbon content of the alloys studied here results in lower solid solution strengthening of austenite by carbon in the bainite transformation temperature range. Lower austenite yield strength would ease the motion of interface dislocation motion during displacive transformation (Olson & Cohen, 1976). Isolating the lowest carbon steels used by Steven & Haynes for special consideration (compositions are given in Table 8.3), it is interesting to note that the driving force at the reported B_S temperatures of these steels is consistently lower than that predicted by the overall relationship between ΔG_M and B_S , determined by considering the complete set of steels, some of which

were of much higher carbon content. Figure 8.11 illustrates the driving force at the reported B_S temperature for these steels lie between the curves representing overall relationship from data of Steven & Haynes and the curve determined for the welding alloys outlined in this chapter. It has been reported (Irvine, Llewellyn & Pickering, 1961) that the solid solution strengthening of austenite by carbon is much potent than that of substitutional alloying elements, therefore it is plausible that the effect of carbon on the required driving force for nucleation of displacive transformation is noticeable over and above its effect of the thermodynamics of the austenite \rightarrow ferrite phase change.

C	Si	Mn	Ni	Mo	Cr	$B_S/^\circ\text{C}$	$\Delta G_m/\text{J mol}^{-1}$
0.19	0.14	1.37	0.56	0.31	0.2	600	-348
0.14	0.19	0.46	3.55	0.12	1.11	550	-444
0.15	0.25	0.41	3.02	0.15	0.9	580	-362
0.11	0.21	0.3	5.04	0.3	0.13	550	-428
0.15	0.2	0.38	4.33	0.17	1.16	500	-634
0.14	0.22	0.5	2.13	0.18	2.00	520	-644
0.19	0.21	0.90	1.87	0.18	1.08	530	-617

Table 8.3 Alloy compositions and driving force values at B_S for the lowest carbon alloys used by Steven & Haynes (1956).

8.5.2 Microstructure

The micrographs of the high-temperature austenitisation specimens are shown in figures 8.3 to 8.6, with those for low temperature austenitisation shown in figures 8.7 to 8.10. Figure 8.3 (a) and (b) shows the microstructure of alloy 116 cooled to room temperature at 5°Cs^{-1} after austenitisation at 1375°C . The higher magnification image clarifies the dense microstructure, showing the very high volume fraction acicular ferrite structure. The same alloy, cooled more slowly and interrupted by quenching at 450°C indicates the uniform formation of acicular ferrite plates (Figure 8.4). In comparison, the alloy 115 specimen cooled at 5°Cs^{-1} shown in Figure 8.5 indicates a greater tendency to form intra-granularly nucleated sheaves, and display a smaller fraction of transformation. Cooling alloy 115 at 0.05°Cs^{-1} and interrupting the cooling by quenching from 400°C reveals very large sheaves in surrounded by large regions of martensite as shown in Figure 8.6.

In contrast to the large austenite grained specimens, the transformation resulting from the low temperature austenitisation was invariably to bainite, though ‘granular bainite’ was

observed at slower cooling rates. Granular bainite does not of course differ from conventional bainite in transformation mechanism, but is a morphological variant which is a consequence of the slow continuous cooling transformation. Figure 8.7 and 8.8 shows the bainitic structures of alloy 116 cooled at 5°Cs^{-1} and $0.5^{\circ}\text{Cs}^{-1}$ respectively. The fraction of transformation is so high that it is difficult to identify individual sheaves. In contrast, the microstructures of the small austenite-grained alloy 115 specimens (Figure 8.9 and 8.10 respectively) show more recognisable sheaves though the specimen cooled at $0.05^{\circ}\text{Cs}^{-1}$ exhibits a granular bainite structure.

These metallographic results can be rationalised by considering the nucleation rates of the alloys at the early stages of transformation. In the coarse grained specimens grain boundary nucleation is all but eliminated, nucleation of acicular ferrite on inclusions being dominant. The more slowly cooled specimens yield the most interesting findings. In the lightly alloyed steel the nucleation rate is high resulting in a uniform distribution of individual plates acicular ferrite. Slower cooling would result in allotriomorphic ferrite formation. In the more highly alloyed steel at very slow cooling the nucleation rate at the onset of transformation is small resulting in the greater importance of auto-catalytic nucleation, hence the presence of intragranularly nucleated sheaves (Fig. 8.6). At higher cooling rates the development of sheaves is inhibited but the rapidly increasing driving force causes further nucleation and results in more hard impingement between plates. The resulting microstructure therefore consists of a fine dispersion of plates showing lower tendency to form sheaves (Fig. 8.5).

In the small grained specimens, the increased grain boundary nucleation rates result in bainitic structures. It is notable again that the formation of recognisable sheaves is more pronounced in the solute-rich alloy 115 which presumably has a lower nucleation rate at the grain boundaries. Granular bainite structures result from the condition in which the extent of transformation is always at its maximum allowable value during the slow cooling. The redistribution of partitioned carbon under these circumstances is enhanced, resulting in the obvious martensitic regions in the microstructures.

8.6 Conclusions

It can be seen from Figure 8.2 that the linear relationship between the driving force required for a detectable rate of nucleation is displayed by the experimental welding alloys for transformation to both acicular ferrite and bainite. This result is significant since it corresponds closely to the published relationship between driving force and onset temperature observed in transformation to Widmanstätten ferrite, and bainite. Acicular ferrite is therefore concluded to nucleate by a similar mechanism to these two phases. It would appear that the mechanism of acicular ferrite nucleation most consistent with these results is that dislocation arrays produced by thermally induced plastic strains around inclusion particles act as the necessary

defects which develop into acicular ferrite nuclei. Such a mechanism is consistent with the fact that both acicular ferrite and bainite nucleate under apparently identical thermodynamic conditions. If nucleation around inclusions were stress-assisted, such close agreement between required driving force for acicular ferrite and bainite nucleation would be merely coincidental, since such stresses are not present at grain boundaries. Similarly, for the proposed case of lattice matching at the inclusion/ferrite interface, the similarity in the required driving force for nucleation of acicular ferrite and bainite, despite the fact that the interface characteristics were very different, would not be expected. The possibility of chemical interaction at the inclusion/austenite interface is again inconsistent with the present findings.

The proposed strain-assisted mechanism for nucleation is consistent with the present findings since it suggests the creation of new, active defects around inclusions which operate in the same way as defects at grain boundaries which give rise to bainite nuclei. The difference in nucleation potency between different chemical species of inclusions is then probably the result of the different amount of plastic strain occurring around the particles during cooling, since the relative thermal contraction between the inclusions and austenite will vary with inclusion species.

The observed microstructures indicate the important role played by the cooling rate in the eventual structure of displacively transformed specimens. High nucleation rates, both on grain boundaries and on inclusions lead to sheaf formation being stifled. In granular bainitic structures the regions left untransformed after cooling to room temperature are more noticeable since the slow cooling rates enable complete redistribution of partitioned carbon resulting in a smaller fraction of trapped carbon between bainitic sub-units.